Aerodynamic performance and stability of insect-inspired flights with flexible wings and bodies

January 2015

Ryusuke Noda

Graduate School of Engineering

CHIBA UNIVERSITY

(千葉大学審査学位論文)

Aerodynamic performance and stability of insect-inspired flights with flexible wings and bodies

January 2015

Ryusuke Noda

Graduate School of Engineering

CHIBA UNIVERSITY

Contents

List of Figures

List of Tables

Abstract

Flexible wings of insects and bio-inspired micro air vehicles generally deform remarkably during flapping flight owing to aerodynamic and inertial forces, which is of highly nonlinear fluid-structure interaction (FSI) problems. To elucidate the novel mechanisms associated with flexible wing aerodynamics in the low Reynolds number regime, I have built up a FSI model of a hawkmoth wing undergoing revolving and made an investigation on the effects of flexible wing deformation on aerodynamic performance of the revolving wing model. To take into account the characteristics of flapping wing kinematics I designed a kinematic model for the revolving wing in two-fold: acceleration and steady rotation, which are based on hovering wing kinematics of hawkmoth, *Manduca sexta*. Our results show that both aerodynamic and inertial forces demonstrate a pronounced increase during acceleration phase, which results in a significant wing deformation. While the aerodynamic force turns to reduce after the wing acceleration terminates due to the burst and detachment of leading-edge vortices (LEVs), the dynamic wing deformation seem to delay the burst of LEVs and hence to augment the aerodynamic force during and even after the acceleration. During the phase of steady rotation, the flexible wing model generates more vertical force at higher angles of attack (40~60 deg.) but less horizontal force than those of a rigid wing model. This is because the wing twist in spanwise owing to aerodynamic forces results in a reduction in the effective angle of attack at wing tip, which leads to enhancing the aerodynamics performance by increasing the vertical force while reducing the horizontal force. Moreover, our results point out the importance of the fluid-structure interaction in evaluating flexible wing aerodynamics: the wing deformation does play a significant role in enhancing the aerodynamic performances but works differently,

which is mainly induced by inertial force in acceleration but by aerodynamic forces in steady rotation.

In addition to the study on the flexible revolving wing, the hovering flight of a hawkmoth, *Agrius convolvuli* are recorded with five synchronized high-speed video cameras as the study on the flexile flapping wing. The integrated method of the filming and reconstruction of a three-dimensional wing model involving both wing kinematics and deformations have been developed with the aim of establishment of a realistic flapping flexible wing model with sufficient precision. Our results show that the wing deformations of the reconstructed wing model in the present study have larger values than that of the past studies. Moreover, single-flapping wing computation are tested with an *in-house* biology-inspired numerical flight simulator. In the comparative study of dynamically morphing and flat wing model, our result show that the wing deformation enhance not only the aerodynamic force but also the flight efficiency which is defined with the vertical force and power.

Finally, the flexibility of the body was focused. The position and attitude controls of flapping wing flyers are challenging because of their inherent instabilities. Insects can cope with such difficulties by finely and quickly tuning their wing kinematics. In addition, it is known that insects change their posture through the joint between thorax and abdomen in response to visual stimuli. In this study, the effect of the body flexion on the flight dynamics of a hovering hawkmoth are investigated numerically by using an *in-house* computational fluid dynamics (CFD) and a flexible body dynamics (FBD) solvers. For an integrated understanding of the effects of the body flexion, the curved or flexible body models, which replicate the longitudinal active and passive body flexion respectively, are developed. Our computational results indicate that the slight change of the center of mass (CoM) caused by the active body flexion alters the total aerodynamic torque, which result in the large pitch-up or pitch down of the body within a few wingbeat cycles. It is also found that, even though the rigid body pitches up in free-flight with a measured wing kinematics, the mild flexibility in the body can maintain the body attitude without any control. These results point out the importance of

the CoM position on the flight dynamics and control of a flapping flight and, furthermore, the possibility of the simple but effective flight-control system with the body flexion for a bio-inspired MAV.

Acknowledgements

I would like to thank, firstly, my advisor Professor Hao Liu who has guided me to the world of biomechanics in animal flight and given me the opportunity to work on a fascinating subject. I benefited a lot from his excellent supervision during my Master and Ph. D. I learnt so much from his not only the proffesional knowledge but also the courage to challenge and face difficulty in scientific research.

I sincerely thank Prof. Masahiro Takei, Prof. Shigeru Sunada, Prof. Ken-ichi Tsubota and Prof. Masanori Ota for serving as the committee members and for providing many precious and fruitful suggestions.

I would like to thank to following people in the Liu laboratory, Dr. Toshiyuki Nakata and Dr. Masateru Maeda for valuable discussions and giving me so many helps throughout th years, and Mr. Li Gen for his advice on writing papers, and Mr. Takashi Fujiwara for his efforts maintaining our computers. I am also grateful to all the members of Biomechanical Engineering Laboratory for all their help, ideas and camaraderie.

Finally, I would like to thank my parents for their support and encouragement during my time at Chiba University.

This work was partly supported by the Grant-in-Aid for Scientific Research (21360078 and 18100002) and Grant-in-Aid for Scientific on Innovative Areas (24120007, JSPS).

Chapter 1
General introduction

Insects and birds have high flight abilities and can maintain the stable flight in the nature with the various environmental disturbances (Combes, et al., 2010, Siegert, et al., 2013, Ravi, et al., 2013, Mountcastle and Combes, 2014). It is also known that most of insects and birds have a flexible structure on their wings and body and these deformable structure can change shape passively on the wing (Young, et al., 2009, Du and Sun, 2010, Tanaka, et al., 2011, Zheng, et al., 2013, Mountcastle and Combes, 2013) and actively/passively on the body (Camhi, 1970, Kammer, 1971, Götz, et al., 1979, Zhanker, 1988, Baader, 1990, Fry, et al., 2003, Luu, et al., 2011, Hinterwirth and Daniel, 2010, Dyhr et al., 2013) and dynamically during flapping flight while flights with fixed-wing and rotary-wing are generally given rigid wings. These deformable structures of insects have attracted attentions from researcher in either biology (Combes and Daniel, 2003, Shyy and et al., 2010, Zhao and et al., 2011) or engineering (Hinterwirth and Daniel, 2010, Tanaka and Shiroyama, 2010, Marardika, et al., 2011, Nakata and Liu, 2012) and it is also known the flexibility of the wing and body affect on aerodynamics, flight dynamics and flight stability (Nakata and Liu, 2012, Kim and Han, 2012, Yokoyama, et al., 2013).

Studies on the flapping flight mechanisms of insects have been around for a long time (Walker, 1931, Maxworthy, 1971, Weis-fogh, 1973, Bennett, 1977, Maxworthy, 1979, Spedding and Maxworthy, 1986, Ellingtion, 1996). In the past, a dynamically scaled mechanical robots has been used for the investigation the flow structure around the wing and the measurement of the aerodynamic/inertial forces. However there were

some difficulties in the quantitative evaluation. Recently, these studies have been begun analyzing with numerical method by many researchers with advances in computational methods. The three-dimensional computational fluid dynamics (CFD) study on the flapping flight was firstly conducted by Liu (Liu, et al., 1998). In this study, a full Navier-Stokes simulation using a finite volume method was solved with a hawkmoth, *Manduca sexta* model. Then the number of research in three-dimensional CFD for investigation of the unsteady flows in the near-/far-fields (Wang, 2000, Liu, 2002, Ramamurti and Sandberg, 2002, Sun and Gang, 2003, Miller and Peskin, 2004, Aono, et al., 2008) has been increased gradually. Moreover, these CFD analysis was coupled with a body dynamics/computational structural dynamics (CSD) analysis (Sun, et al., 2007, Wu, et al., 2009, Nakata and Liu, 2012, Kim and Han, 2014) and it has been approaching to reproduce the more realistic flapping fight in the computational study.

In the present paper, I focus on the flexibility of the wing and body of a hawkmoth and these effects on aerodynamics, flight dynamics and flight stability have been investigated numerically/experimentally. In Chapter 2, the flexible revolving wing computations with an *in-house* fluid-structure interaction (FSI) solver was conducted for elucidating the novel mechanisms associated with flexible flapping wings. In Chapter 3, the method of the digitizing and reconstruction of the wing kinematics and deformations was developed with high-speed video cameras and a hawkmoth, *Agrius convolvuli* for reconstructing the dynamically morphing wing model with sufficient precision. Finally in Chapter 4, a flexible multi body dynamics solver with a three-dimensional flexible beam model was developed newly and coupled with an *in-house* CFD solver. Using this integrated simulator, the active/passive effect of the body flexibility has been investigated with hawkmoth body model.

Chapter 2
Revolving wing : Aerodynamic performance of rigid and flexible wings

2.1 Introduction

Insect's inherent flexible wings and flapping-winged micro air vehicles (MAV) are generally shaped thin and flat with light structures. These bio-flyers and bio-inspired MAVs flap their wings with high flapping frequencies to stay airborne, and within each beat cycle flapping wings repeat acceleration and deceleration. These wings normally are deformed mainly due to inertial and aerodynamic forces. This is of highly nonlinear fluid-structure interaction (FSI) problems. Many studies relating flexible wing aerodynamics have been undertaken (Young, et al., 2009, Du and Sun, 2010, Tanaka, et al., 2011, Mountcastle and Combes, 2013, Zheng, et al., 2013) till now, however they mostly focused on flapping wing aerodynamics with prescribed wing deformations. The wing deformation based on the FSI analysis and its effect on flapping flexible wing aerodynamics and energetics are still a main subject because there is the complexity of nonlinear interactions between flapping wing aerodynamics and structural dynamics (Nakata and Liu, 2012).

Recently, aerodynamics of revolving wing models have also been a subject as a simplified model for flapping wings. This study is conducted either by means of dynamically scaled mechanical robots (Dickinson, et al., 1999, Usherwood and Ellington, 2002, Lentink and Dickinson, 2009) or by computational fluid dynamic

models (Zheng, et al., 2013, Harbig, et al., 2013) in the low Reynolds number regime. These models present the general aerodynamic performance of a flapping wing by force coefficients that can be estimated with blade element models, and the effects of wing planform shape, twist and camber on the revolving wing aerodynamics can be further investigated in a separated way (Usherwood and Ellington, 2002, Zheng, et al., 2013, Harbig, et al., 2013). Such revolving wing models with a simplified kinematics may be an essential model for an integrated understanding of the essence of flapping wing aerodynamics in a manner of separating some novel mechanisms such as the LEV and other force enhancement mechanisms from the complexity of flapping wing systems.

In this study, I aim at establishing a FSI model of a revolving insect wing to tackle the nonlinear FSI problem associated with flexible wing aerodynamics at low Reynolds numbers. Follow our previous computational FSI analysis (Nakata and Liu, 2012) of flexible flapping wing aerodynamics that utilized a realistic morphological and structural model of hawkmoth wing, I constructed our revolving wing kinematics on the basis of the realistic wing kinematics of a hovering hawkmoth with a Reynolds number and the characteristics of acceleration identical to those of the hovering hawkmoth (Nakata and Liu, 2012). The kinematic model for the revolving wing is designed in two-fold: acceleration and steady rotation, in which the wing is accelerated around a pivot at wing base from rest and continues steady rotation after reaching the mean angular velocity of a hovering hawkmoth. The wing deformation, and the vertical and horizontal forces of the flexible revolving wing are simulated and compared with those of a rigid revolving wing. I further give an extended discussion on wing aerodynamics and energetics during the phases of acceleration and steady rotation and its correlations with wing deformations as well as its discrepancy compared with flapping wings.

2.2 Methods

2.2.1 Morphological wing model and revolving wing kinematics

In this study, I use a hawkmoth wing model that was originally developed by Aono and Liu (2006) on the basis of the two-dimensional digitized image of hawkmoth,

Agrius convolvuli. The wing length R and mean chord length c_m are 5.05 and 1.83 cm, respectively. Figure 2.1 shows the hawkmoth wing model and the coordinate system used in this study.

The inertial force as well as aerodynamic force can have significant effects on wing deformations (Combes and Daniel, 2003). Therefore, the kinematic model of a revolving wing is constructed by simplifying the realistic wing kinematic of a hovering hawkmoth so that the Reynolds number and acceleration of the wing can be same with that of the hawkmoth's wing in hovering. The angular velocity of revolving wing ω is defined as follows:

$$w(t) = \begin{cases} \Omega \cos\left(\frac{1}{2}\left(1+\frac{t}{T_{accel}}\right)\pi\right), & t < T_{accel} \\ \Omega, & T_{accel} \geq t \end{cases} \qquad (2.1)$$

where Ω is rotational angular velocity, t is dimensionless time and T_{accel} is the time when the wing terminates its acceleration and starts steady rotation. In this study, T_{accel} is defined by using the wing kinematics of a hovering hawkmoth, *Manduca sexta* (Aono and Liu, 2006, Willmott and Ellington, 1997). As shown in figure 2.2, the wing tip velocity reaches its maxima when the flapping-wing tip acceleration of the hovering hawkmoth becomes zero at about 0.15 flapping period, which is identical to a dimensionless time of approximately1.64 after stroke reversal. I utilize this value as T_{accel} in equation (2.1). The rotational velocity Ω in equation (2.1) is calculated to be 104.41 rad/s. The time-history of the angular velocity ω during the acceleration phase is also plotted in figure 2.2. The wing model keeps rotation up to three revolving cycles after T_{accel} during the phase of steady rotation. The Reynolds number Re is defined as $Re = U_{ref}\, c_m/\nu$, where U_{ref} is reference velocity and ν is the kinematic viscosity of air (1.5×10^{-5} m^2/s). The mean chord length c_m is used as the reference length, and the U_{ref} is defined as ΩR, the wing tip velocity of the rigid wing in steady rotation. Hence, Re is calculated to be approximately 6,400.

2.2.2 Fluid-structure interaction (FSI) model

Analysis of the flexible revolving wing aerodynamics was conducted with an *in-house* fluid-structure interaction (FSI) solver developed by Nakata and Liu (2012). This FSI solver consists of a computational fluid dynamics (CFD) solver based on a fortified Navier-Stokes solver (Liu and Kawachi, 1998, Liu, 2009) and a computational structural dynamic (CSD) solver (Nakata and Liu, 2012) based on the finite element method specialized for thin structure such as insect wing. The CFD and CSD solvers are coupled in a manner of loose coupling. More details can be found in Nakata and Liu (Nakata and Liu, 2012). Note that the hawkmoth body model, which was used as a global grid in previous studies, is replaced with a sufficient small cylinder, which has been confirmed having negligible influence on the revolving wing aerodynamics. Both CFD grids and CSD meshes used in this study are illustrated in figure 2.3.

2.2.3 Computational fluid (CFD) dynamics solver

A general formulation of the multi-blocked, overset grid, fortified solutions to the Navier-Stokes equations is performed in the global system (*X, Y, Z*) as depicted in figures 2.3a and 2.3b. The algorithm employed here is based on a single Navier-Stokes solver as in Liu and Kawachi (Liu and Kawachi, 1998) but is extended to a multi-blocked, overset-grid system by means of the fortified solution algorithm (Liu, 2009). The governing equations are the three-dimensional, incompressible, unsteady Navier-Stokes equations written in strong conservation form for mass and momentum. The artificial compressibility method is used by adding a pseudo time derivative of pressure to the equation of continuity. For an arbitrary deformable control volume *V(t)*, the non-dimensionalized governing equations are

$$\int_{V(t)} \left(\frac{\partial \mathbf{Q}}{\partial t} + \frac{\partial \mathbf{q}}{\partial \tau} \right) dV + \int_{V(t)} \left(\frac{\partial \mathbf{F}}{\partial x} + \frac{\partial \mathbf{G}}{\partial y} + \frac{\partial \mathbf{H}}{\partial z} + \frac{\partial \mathbf{F}_v}{\partial x} + \frac{\partial \mathbf{G}_v}{\partial y} + \frac{\partial \mathbf{H}_v}{\partial z} \right) dV \quad , \tag{2.2}$$

where

$$\mathbf{Q}=\begin{bmatrix}u\\v\\w\\0\end{bmatrix},\mathbf{q}=\begin{bmatrix}u\\v\\w\\p\end{bmatrix},\mathbf{F}=\begin{bmatrix}u^2+p\\uv\\uw\\\lambda u\end{bmatrix},\mathbf{G}=\begin{bmatrix}vu\\v^2+p\\vw\\\lambda v\end{bmatrix},\mathbf{H}=\begin{bmatrix}wu\\wv\\w^2+p\\\lambda w\end{bmatrix},\mathbf{F_v}=-\frac{1}{Re}\begin{bmatrix}2u_x\\u_y+v_x\\u_z+w_x\\0\end{bmatrix},\mathbf{G_v}=-\frac{1}{Re}\begin{bmatrix}v_{x+}u_y\\2v_x\\v_z+w_y\\0\end{bmatrix},\mathbf{H_v}=-\frac{1}{Re}\begin{bmatrix}w_{x+}u_z\\w_{y+}v_z\\2w_z\\0\end{bmatrix}.$$

In the preceding equations, λ is the pseudo-compressibility coefficient; p is pressure; u, v, and w are velocity components in Cartesian coordinate system X, Y, and Z; t denotes physical time while τ is pseudo time; and Re is the Reynolds number. Note that the term $\boldsymbol{q}$ associated with the pseudo time is designed for an inner-iteration at each physical time step, and will vanish when the divergence of velocity is driven to zero so as to satisfy the equation of continuity.

The fortified Navier-Stokes solution algorithm is achieved by adding forcing terms to the Navier-Stokes equations; by introducing the generalized Reynolds transport theorem and by employing the Gauss integration theorem, an integrated form of the equation (2.4) in general curvilinear coordinate system is obtained as

$$\int_{V(t)}\frac{\partial\mathbf{q}}{\partial\tau}dV+\frac{\partial}{\partial t}\int_{V(t)}\mathbf{Q}dV+\oint_{S(t)}\left(\mathbf{f}-\mathbf{Q}\mathbf{u}_g\right)\bullet\mathbf{n}dS=\sigma\left(\mathbf{q}_f-\mathbf{q}\right) \qquad (2.3)$$

,

where $\mathbf{f}$ = (F+F_v, G+G_v, H+H_v); S(t) denotes the surface of the control volume; $\boldsymbol{n}$=(n_x, n_y, n_z) are components of the unit outward normal vector corresponding to all the faces of the polyhedron cell; $\boldsymbol{u_g}$ is the local velocity of the moving cell surface. The switching parameter σ is set to be sufficiently large, compared to all the other terms in the region, and where the solution $\boldsymbol{q_f}$ is available by the subset equations, and zero outside the region. For $\sigma >> 1$, the added source term simply forces $\boldsymbol{q} = \boldsymbol{q_f}$; otherwise it blends $\boldsymbol{q}$ with $\boldsymbol{q_f}$. When $\sigma = 0$, the equations go back to the ordinary Navier-Stokes equations.

The solutions to the multi-blocked, overset grid Navier-Stokes equations require specific boundary conditions at the overlapping zone stencils among grids, at the solid walls of a revolving wing and a cylinder as well as at the far field outside boundary as

shown in figure 2.3a. For two single grid blocks, the fortified Navier-Stokes equations were solved two times at each time step (Liu, 2009). For the holes inside the grid and the outermost two grid points, the $\boldsymbol{q_f}$ are specified there by $\boldsymbol{q}$ of overlapping zones with other single grid at previous time step. Inside the computational domain except the holes and the single grid boundary $\boldsymbol{q}$ are equal to $\boldsymbol{q_f}$ by setting $\sigma = 0$.

When the Navier-Stokes equations are solved for each block, the aerodynamic forces $\mathbf{F_{aero}} = (F_{ax}, F_{ay}, F_{az})$ exerted on the wing is evaluated by a sum of aerodynamic forces in the global coordinate system. In this study, the vertical and horizontal forces coefficients C_v and C_h on a revolving wing are defined in the same way as in (Usherwood and Ellington, 2002) such as:

$$C_v = \frac{F_{az}}{\rho S_2 \Omega^2}, \tag{2.4}$$

$$C_h = \frac{T_{az}}{\rho S_3 \Omega^2}, \tag{2.5}$$

where F_v is the aerodynamic vertical force on a single wing, T_{az} is the torque about the rotational axis, S_2 and S_3 are the second and third moments of area for a single wing (Ellington, 1984), respectively.

2.2.4 Computational structural dynamic (CSD) solver

In order to simulate dynamics and large deformations of insect wings due to inertial and aerodynamic forces under revolving motion, a finite element method (FEM)-based structural dynamic solver is employed (Nakata and Liu, 2012). To model a thin structure like insect wing, I employ a triangular shell element termed AT/DKT with a very thin and anisotropic structure, which combines an Allman membrane triangular (AT) element with a discrete Kirchhoff triangular (DKT) element (Ertas, et al., 1992). The element is hereby further utilized to study nonlinear dynamic response by introducing an updated Lagrangian (UL) formulation (Bathe, et al., 1975, Mohan and Kapania, 1998). The virtual work principle for a single element at time $t+\Delta t$ can be expressed as

$$\int \delta\boldsymbol{\varepsilon}^T \mathbf{s} dV + \int \rho_s \delta \mathbf{R}^T \ddot{\mathbf{R}} dV = \delta W_e \tag{2.6}$$

where ρ_s is the density of a wing; **R** is the position in reference to the origin of the global coordinate system at time $t+\Delta t$; s and **ε** are the vectors of second Piola-Kirchhoff stress and incremental Green-Lagrange strain form the configuration at time t to the configuration at time $t+\Delta t$, respectively; δW_e is the virtual work done by external forces **F** such as fluid force. By using the nodal displacement due to elastic deformation in reference to the wing base-fixed frame $\mathbf{u_s}$ and shape functions of AT/DKT elements (Ertas, et al., 1992), the integrals of equation (2.6), representing the virtual work due to internal and inertial forces in an element, can be given by

$$\int \rho_s \delta \mathbf{R}^T \ddot{\mathbf{R}} dV = \delta \mathrm{u}^{\mathrm{T}} \left(\mathbf{M}\ddot{\mathbf{u}}_s + \mathbf{h} \right), \tag{2.7}$$

$$\int \delta\boldsymbol{\varepsilon}^T \mathbf{s} dV = \delta \mathrm{u}^{\mathrm{T}} \left(\mathbf{K}\mathbf{u}_s + \mathbf{f}_i \right), \tag{2.8}$$

where **K** is the tangent stiffness matrix; **M** is the consistent mass matrix; $\mathbf{f_i}$ is the internal force vector; **h** represents the inertial forces by prescribed flapping motion. The equilibrium equation given by substituting equations (2.7) and (2.8) into equation (2.6) is assembled to form the global incremental equilibrium equation. The nonlinear equation of motion is solved by using the Newton-Raphson method combining with Wilson θ integration scheme, which may be expressed as

$$\mathbf{K}^{(i-1)} \Delta \mathbf{u}_s^{(i)} = \mathbf{F} - \mathbf{f}_i^{(i-1)} - \mathbf{M}\ddot{\mathbf{u}}_s^{(i-1)} - \mathbf{h}_e \tag{2.9}$$

where $\mathbf{u_s}^{(i)} = \mathbf{u_s}^{(i\text{-}1)} + \Delta \mathbf{u_s}^{(i)}$. The superscripts of $\mathbf{K}^{(i\text{-}1)}$ and $\mathbf{f_i}^{(i\text{-}1)}$ denote the previous time of i-1 when $\mathbf{u_s}^{(i\text{-}1)}$ (Bathe, et al., 1975).

2.3 Results and Discussion

2.3.1 Force generation in rigid and flexible revolving wings

Figure 2.4a-b show time courses of vertical and horizontal force coefficients plotted against angles of wing revolution. Non-dimensional time is depicted on the horizontal axis for reference. It is seen that the aerodynamic forces of both rigid and flexible wings show a rapid increase immediately after the onset of wing revolution, which is more obvious at higher angles of attack (40 ~ 60 deg.) due to the added mass. Note that the aerodynamic forces are apparently enlarged in the flexible wing during the acceleration phase (An extensive discussion on discrepancy between rigid and flexible wing will be given in section 2.3.3). The aerodynamic forces are relatively stable after the unsteady (acceleration) phase (0-180 deg.) but turn to decrease gradually after 360 deg. when the wing encounters and passes through the downwash generated during the first cycle. A bigger drop in both vertical and horizontal forces is then observed at higher angles of attack (40 ~ 60 deg.). As postulated by Usherwood and Ellington (2002) a full development of the vortex-structured wake with its associated radial inflow over the wing can shift the position of vortex breakdown inwards under steady rotational conditions at higher angles of attack and hence lead to a reduction in vertical force. At lower angles of attack (10 ~ 20 deg.), both vertical and horizontal forces converge comparatively faster and then keep almost constant without fluctuations till 1080 deg. Such decreasing in aerodynamic forces are continuously observed from 360 to 720 deg. but then the aerodynamic forces turn out to be unstable fluctuating largely at larger angles of arrack even though the wake is fully developed after the second cycle. Such time-varying feature of aerodynamic forces against angles of attack is also observed in experimental studies (Dickinson, et al., 1999, Usherwood and Ellington, 2002). For the sake of discussion, I have defined the interval from 0 to 180 deg. as unsteady (acceleration) phase, and the interval from 720 to 1080 deg. as steady (rotation) phase, and the averaged forces during each interval will be used for the following discussions.

2.3.2 Wing deformation in flexible revolving wings

Twist and spanwise bending at 0.8R are further plotted against angle of wing revolution as illustrated in figure 2.4c-d. Note that the twist angle θ_{tw} and the spanwise bending angle θ_b are defined in a wing base-fixed coordinate system as depicted in figure 2.5. Both the twist and spanwise bending are observed increasing with increasing angle of attack throughout most of the period of the simulation. During the acceleration phase, the wing changes its shape rapidly and the wing deformation is maximized around a phase of 20 deg., where the largest twist and spanwise bending are approximately 7.2 deg. and 8.6 deg., respectively. Such large wing deformation is thought due to the large inertial forces (Combes and Daniel, 2003) as well as the large aerodynamic forces as described in the preceding section. Then the wing rapidly returns to its original flat shape until a phase of 50 deg. and eventually converges to some level around 180 deg. after experiencing some slight fluctuations. Corresponding to the time courses of aerodynamic forces in figure 2.4a-b the twist and spanwise bending also demonstrates a pronounced decrease during the interval from 360 to 720 deg. Note that at higher angles of attack slight fluctuations in twist and spanwise bending are observed after 540 deg., which are induced by the unstable vertical and horizontal forces as shown in figures 2.4a-b.

2.3.3 Aerodynamic performance during unsteady phase

Figure 2.6 shows the time-averaged vertical force coefficients C_v, horizontal force coefficients C_h, and their ratios C_v/C_h versus angles of attack. Note that these time-averaged value were calculated by using each time-varying value in the two-interval (unsteady and steady phases) as shown the shaded areas in figure 2.4. Table 2.1 further gives those values at four angles of attack. During the unsteady phase when the wing rotates from 0 up to 180 deg., the vertical force coefficient increases with increasing angle of attack till the AoA of 40 deg. but then shows a drop at the AoA of 60 deg. The horizontal force coefficient, however, shows a monotonic increase at four angles of attack. Such correlation between the time-averaged force and angle of attack is

also observed by Dickinson et al. (1999) and by Usherwood and Ellington (2002). Note that this tendency is also seen here in the case of the flexible wing. I further compare the discrepancy between rigid and flexible wings. Interestingly, I see that the FSI-based wing deformations lead to a reduction of horizontal force coefficients at all four angles of attack as shown in figure 2.6a and in table 2.1. The vertical force coefficients (figure 2.6b), however, show a divergent result: the flexible wing underperforms the rigid wing at lower angles of attack of 10-20 deg. but outperforms the rigid wing at higher angles of attack of 40-60 deg. Furthermore, the vertical-to-horizontal force ratio C_v/C_h of the flexible wing outperforms the rigid wing at all four angles of attack (figure 2.6c). Our results demonstrate that the flexible wing undergoing revolving is capable to achieve better aerodynamic performance during the unsteady (acceleration) phase. Moreover, it is interesting to find that the vertical-to-horizontal force ratio shows a pronounced increase with increasing the angle of attack with a net increase of 9.3, 12.7, 14.0, 15.0% compared with that of the rigid wing at the angle of attack of 10, 20, 40, 60 deg., respectively.

Here I further take one case at angle of attack of 40 deg. for instance to give an extensive discussion on aerodynamic performance during unsteady (acceleration) phase. Note that this angle of attack corresponds to the cycle-averaged feathering angle of a flapping wing in hawkmoth hovering, and the corresponding aerodynamic performance of the flexible revolving wing obtained here can be used to predict and analyze that of the flexible flapping hawkmoth wing. As shown in figure 2.7a-b the maximum vertical and horizontal force coefficients produced by the flexible wing are at least 25 percent larger than those of the rigid wing and the timing is obviously largely delayed. Such delayed timing of the maximum aerodynamic forces in the flexible revolving wing actually corresponds with a delayed LEV very similar with that observed in a flapping flexible wing by Nakata and Liu (2012). As illustrated in figures 2.8-2.9 the visualized pressures and spanwise vorticity on upper wing surface completely support such delayed LEV mechanism of the flexible revolving wing model. The pressure contours on upper surfaces of flexible and rigid wings show significant discrepancy as well as the

spanwise vorticity does at 0.5R and 0.8R. Note that the flow visualizations are done at three points of A, B and C (figure 2.7) corresponding to three phase angles of wing revolution of 23.74, 31.06, and 38.27 deg., respectively. In addition, as can be seen in figure 2.7c-d and figure 2.9A-C, the twist and spanwise bending in the flexible wing result in some pitch-up rotation at wing tip, which is likely capable to stabilize the LEVs and hence to enhance the generation of both vertical and horizontal forces.

2.3.4 Aerodynamic performance during steady phase

During the steady phase when the wing rotates from 720 up to 1080 deg. as shown in figure 2.6 and Table 2.2 the plots of force coefficient against angle of attack show similar tendency with that of the unsteady phase; the flexible wing outperforms the rigid wing at higher angles of attack of 40-60 deg. and is capable to achieve better aerodynamic performance. Here the vertical-to-horizontal force ratio also shows a pronounced increase with increasing the angle of attack with a net increase of 3.0, 14.3, 11.5, 10.3% compared with that of the rigid wing at the angle of attack of 10, 20, 40, 60 deg., respectively.

Note that the time-varying force coefficients and wing deformations, at higher angles of attack of 40-60 deg., show comparatively large fluctuations in both flexible and rigid wings (figures 2.4a-b). Such fluctuating feature observed in the aerodynamic forces is probably caused by the breakdown and shedding of LEVs and tip vortices, which may result in some unstable vortex structures at wing tip. Liu, et al. (Liu, et al., 1998) pointed out that the tip vortex generates some reverse pressure gradient on the wing surface and hence creates a reverse axial flow in the half of the down-stroke; Harbig, et al. (Harbig, et al., 2013) reported that as Reynolds number increases, the LEV tends to evaluate to two co-rotating vortex structures with a smaller counter-rotating vortex created as well as some adverse pressure gradient through the core of the vortex.

Again with consideration of the case at angle of attack of 40 deg. in order to give an extensive discussion on aerodynamic performance during the steady phase, I find that the vertical force coefficient of the flexible wing is slightly higher than that of the rigid

wing but the horizontal force coefficient is approximately 10% lower. Furthermore, it is seen that the slight fluctuations in twist and spanwise bending are less than 1.0 deg., which should have less influence on the flow structures. These are supported as shown in figures 2.10-2.11 by the visualized pressure contours and spanwise vorticity of flexible and rigid wings at three angles of wing revolution of 802, 904 and 997 deg., in which the discrepancy between flexible and rigid wings is margin. Figure 2.12 shows time courses of local angle of attack of the flexible wing from wing base to wing tip at AoA of 40 deg. At positions of 0.2R and 0.4R, the local angle of attack is reduced merely less than 1.0 deg. but when the position is greater than 0.4R the angle of attack shows a reduction by 2.0 to 5.0 deg.

2.4 Summary

In this study, the effects of wing deformation on aerodynamic performance of a revolving insect wing model are investigated by using a hawkmoth wing model and FSI-based simulations. It is confirmed that the wing flexibility can enhance the aerodynamic performance of the flexible revolving wing both during acceleration (an unsteady phase) that replicates the flapping wing kinematics of a hovering hawkmoth and during steady rotation (a steady phase) particularly when the angle of attack is large sufficient to match the mean feathering angle of a hovering hawkmoth. The flexible wing model can generate much greater aerodynamic forces than the rigid wing does during the acceleration phase because the dynamic wing deformations owing to the wing acceleration that results in large inertial and aerodynamic forces can reduce the angle of attack at wing tip. During the phase of steady rotation, the wing deformation is comparatively smaller but the wing twist can still reduce the angle of attack at wing tip and hence increases the vertical force at higher angles of attack (40~60 deg.) while reducing the horizontal force. Both of these (acceleration-based) unsteady and steady (rotation) mechanisms for the flexible revolving wing model presumably hold more or less for flexible flapping wings as well. Moreover, our results demonstrate that the fluid-structure interaction is important and essential in evaluating the aerodynamic

performance of flexible flapping wings and even in the simplified case of the revolving wing model, the wing deformation due to inertial force / aerodynamic force can enhance the aerodynamic performances but in different manner during acceleration / steady rotation.

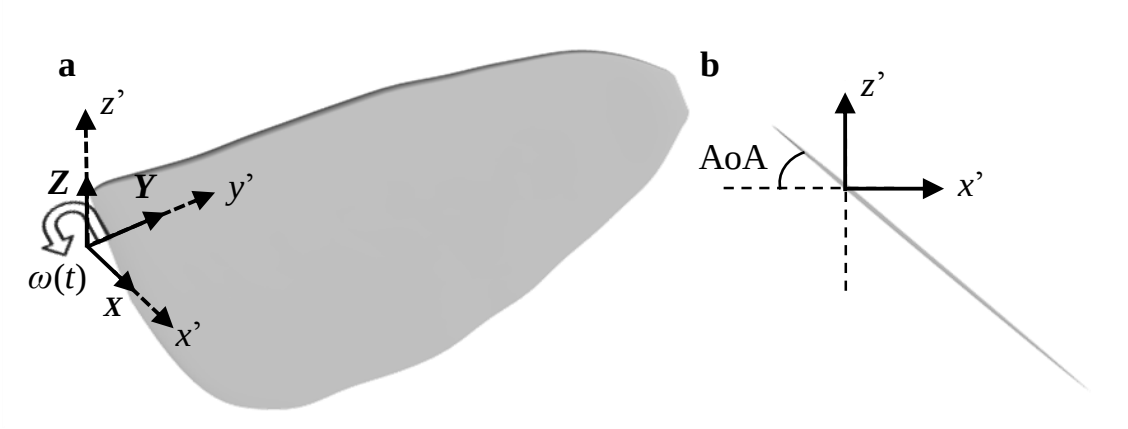

Fig. 2.1 (a) A hawkmoth wing model with a global coordinate system (X, Y, Z) and a wing-fixed coordinate system (x', y', z'); (b) Definition of angle of attack (AoA) at wing base.

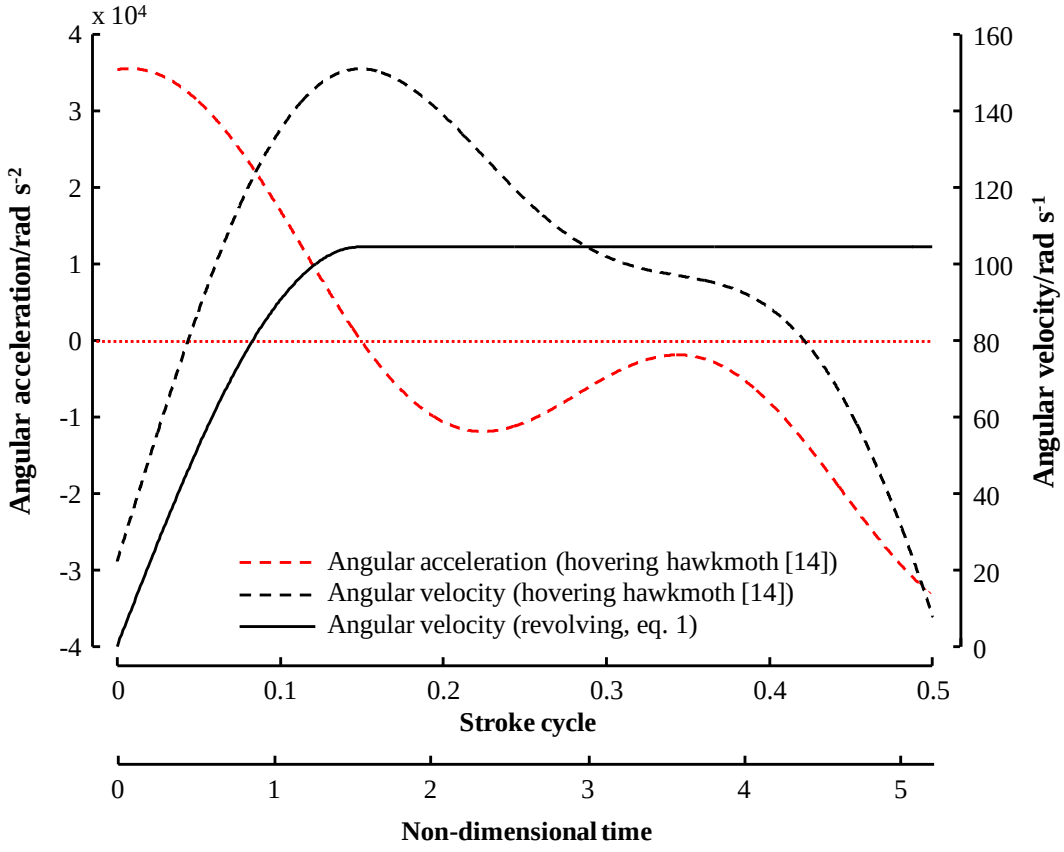

Fig. 2.2 Time courses of angular velocities and accelerations of a flapping hawkmoth wing in hovering (dotted lines), and angular velocity of a revolving hawkmoth wing model (solid black line).

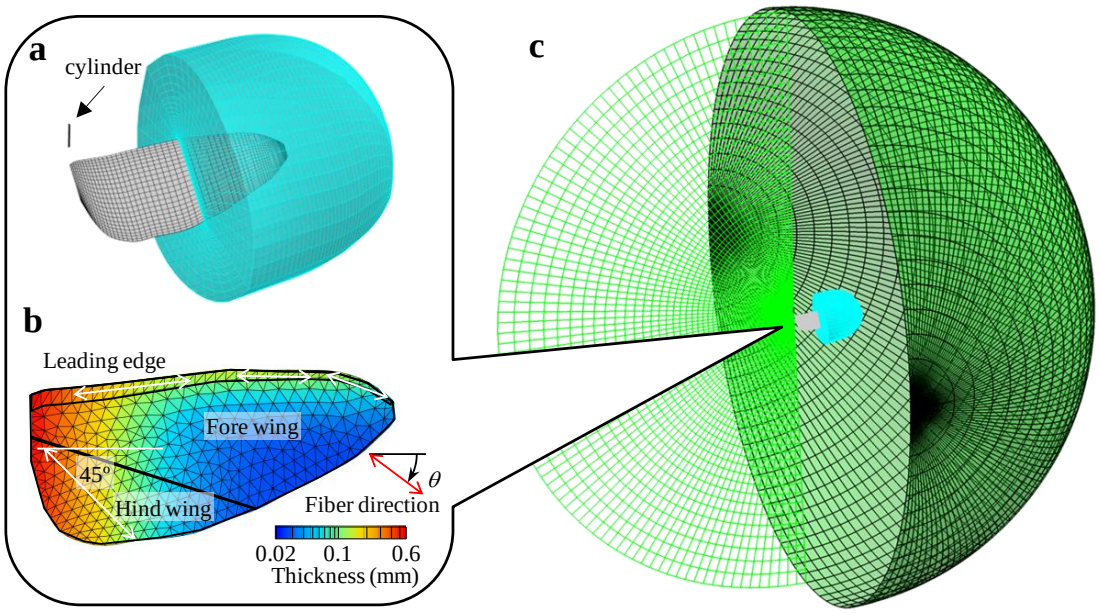

Fig. 2.3 Grid systems. (a) Local grid for CFD analysis; (b) A FEM mesh model of a hawkmoth wing; (c) global grids for CFD analysis. Note that a local tiny cylinder grid is set merely for generating global grids and its influence is negligible.

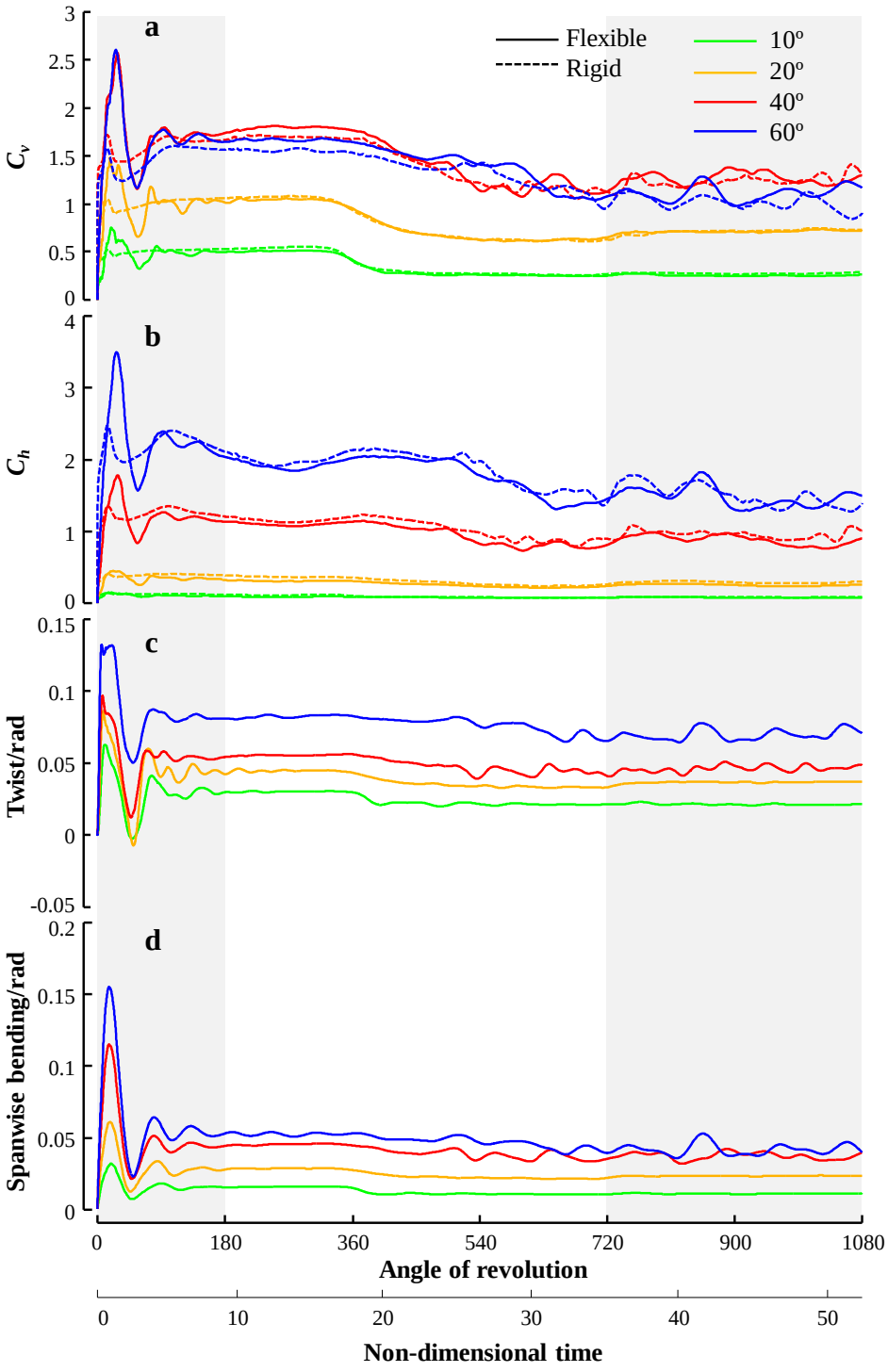

Fig. 2.4 Time courses of (a) vertical and (b) horizontal force coefficients generated by revolving flexible and rigid wings, and (c) twist, (d) spanwise bending of a flexible revolving wing. Shaded area corresponds to unsteady (0-180 deg.) and steady (720-1080 deg.) phases.

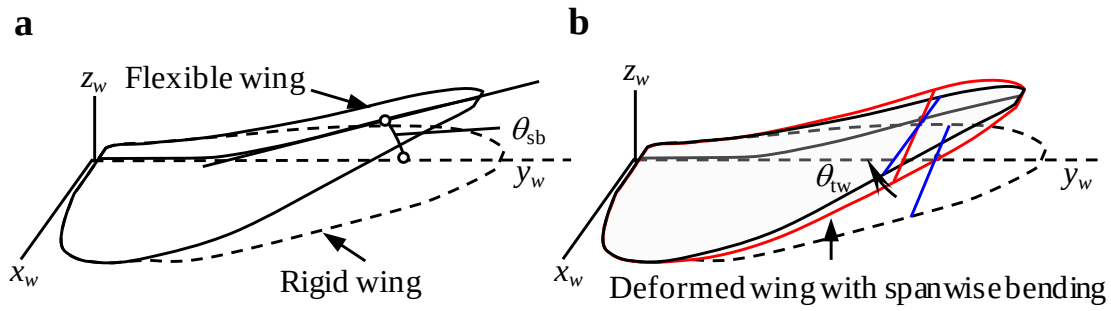

Fig. 2.5 Definition of (a) spanwise bending angle θ_{sb} and (b) twist angle θ_{tw} in a flexible wing. Computed wing deformations are described in a wing base-fixed coordinate system.

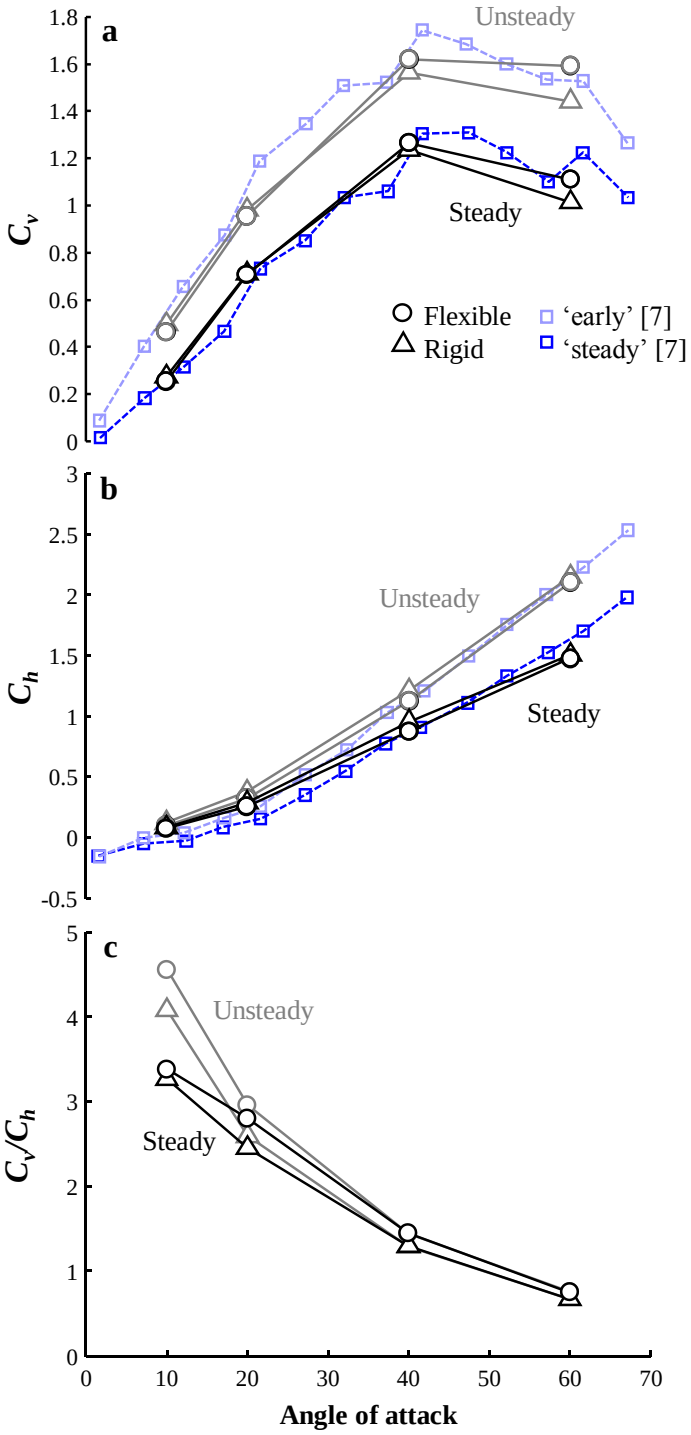

Fig. 2.6 Effects of angle of attack on (a) vertical and (b) horizontal force coefficients, and (c) vertical to horizontal force coefficient ratio in revolving flexible and rigid wings. Experimental results by Usherwood and Ellington (2002) are also plotted for comparison.

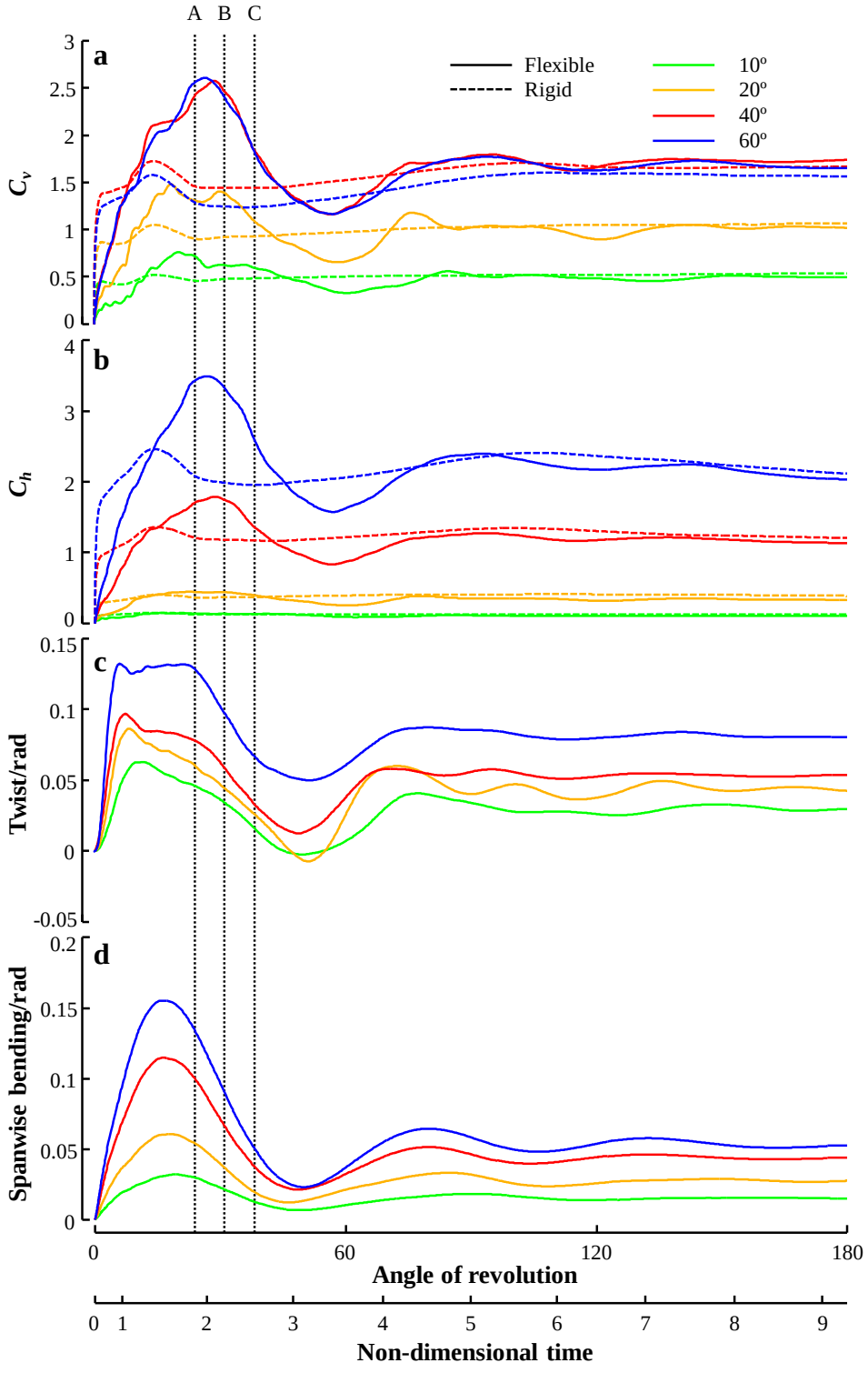

Fig. 2.7 Time courses of (a) vertical and (b) horizontal force coefficients of revolving flexible and rigid wings, and (c) twist, (d) spanwise bending of a flexible revolving wing during unsteady phase.

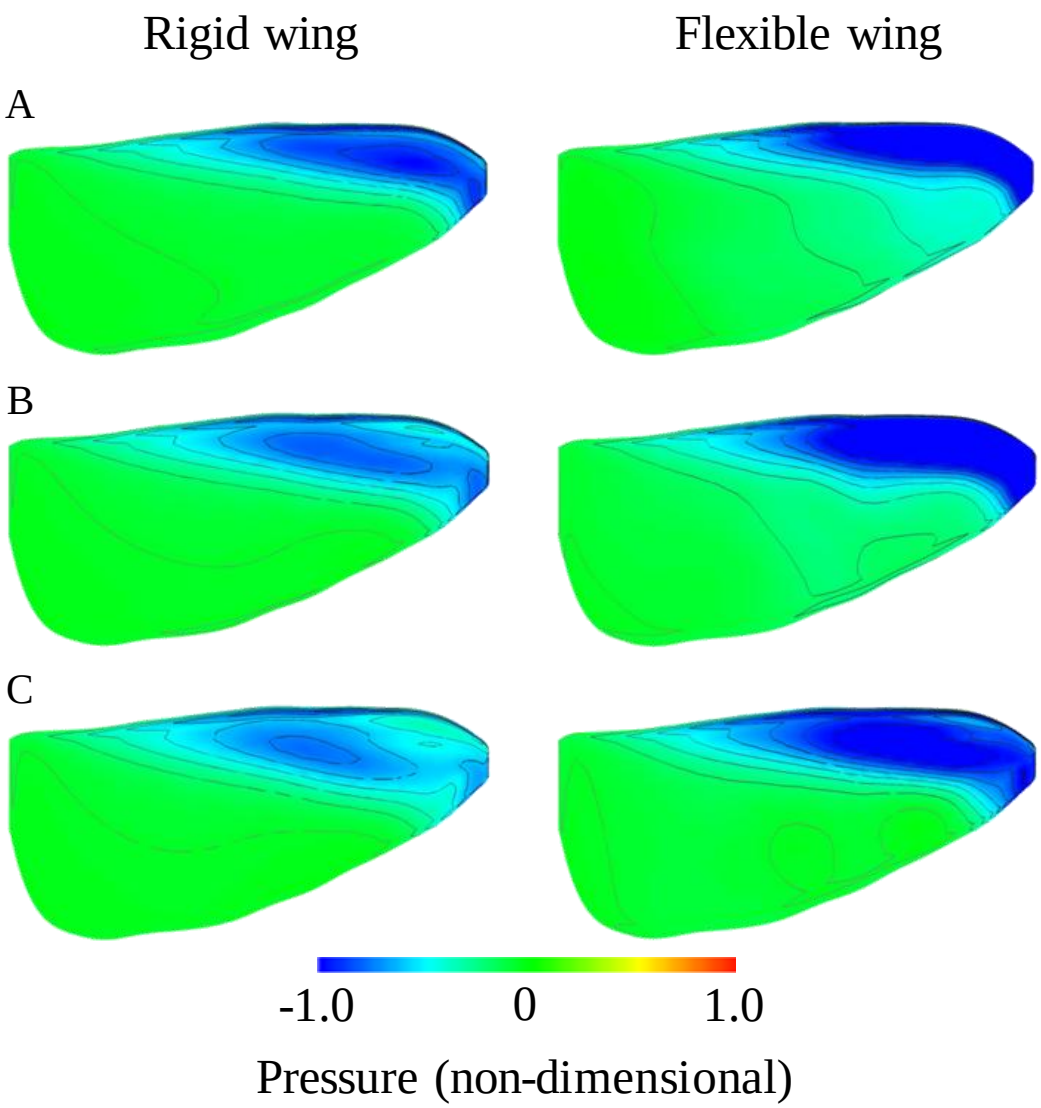

Fig. 2.8 Pressure contours on upper surfaces of flexible and rigid wings at instants A- C in Fig. 2.7.

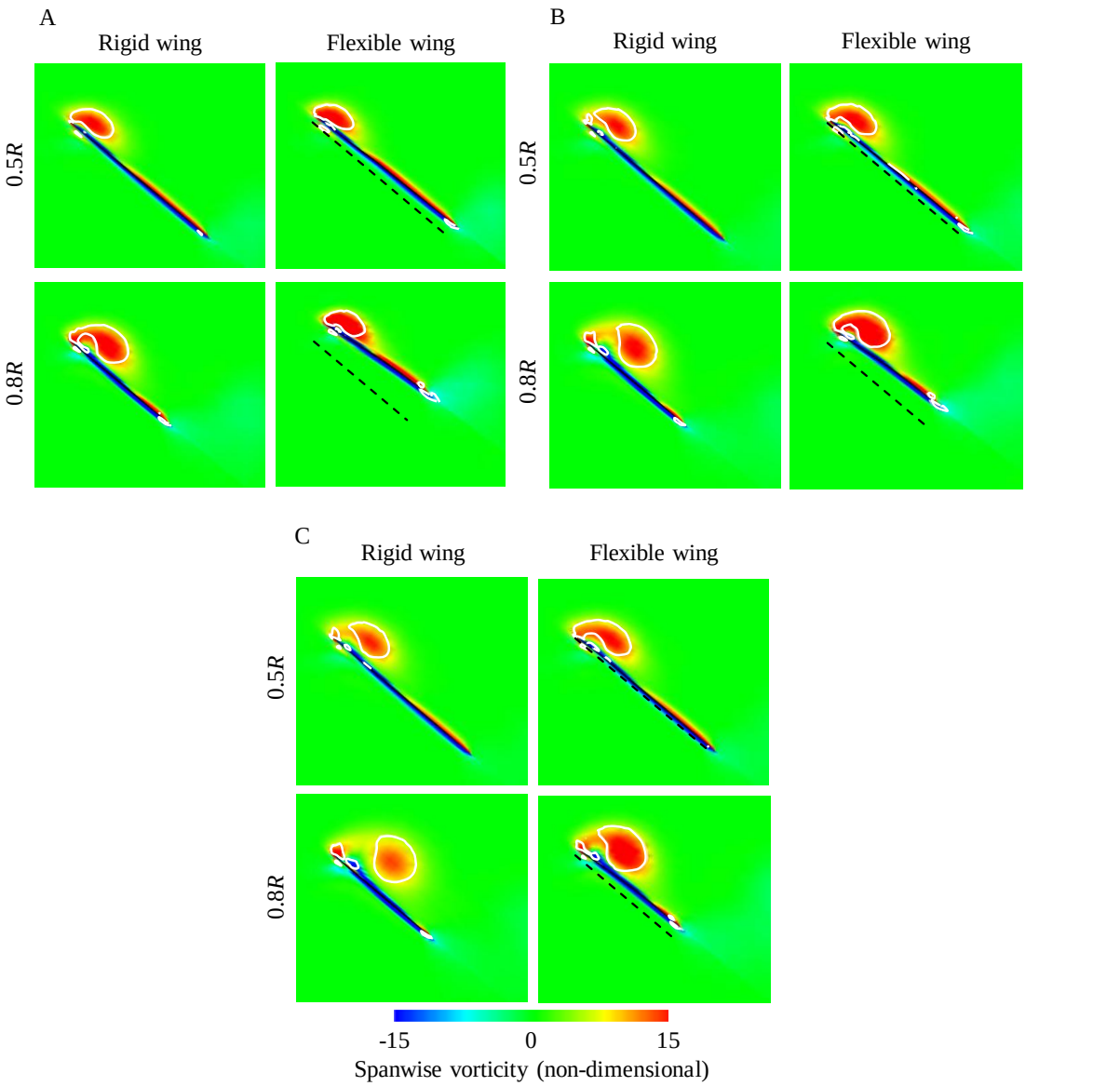

Fig. 2.9 Spanwise vorticity around rigid and flexible wings at instants A-C (Fig. 2.7) with AoA of 40 deg. Cross-section of a rigid wing is superimposed in the results of flexible wing by dotted line for comparison. White solid lines represent contours of constant Q criterion.

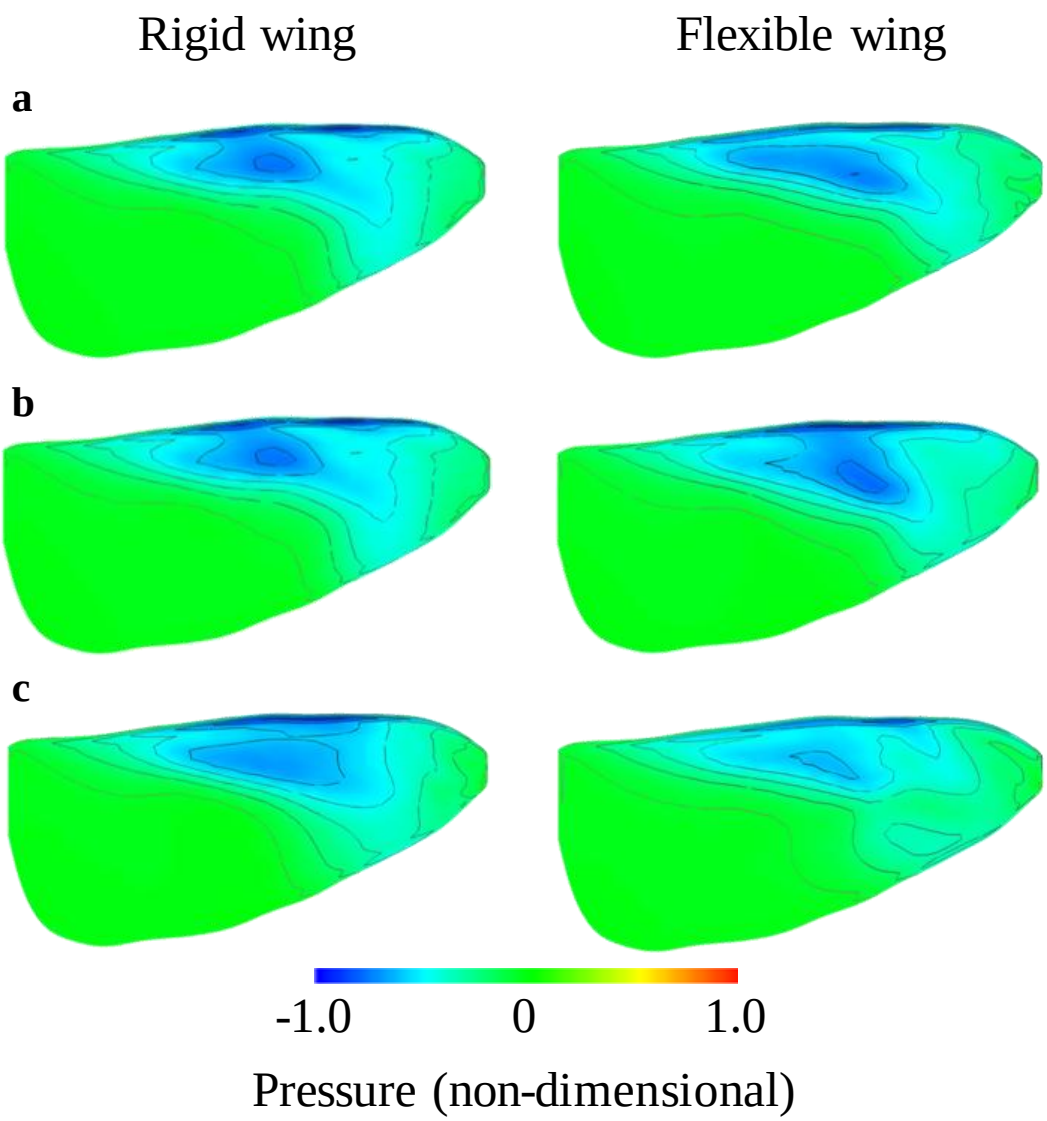

Fig. 2.10 Pressure contours on upper surfaces of flexible and rigid wings at angle of wing revolution of (a) 802; (b) 904 and (c) 997 deg.

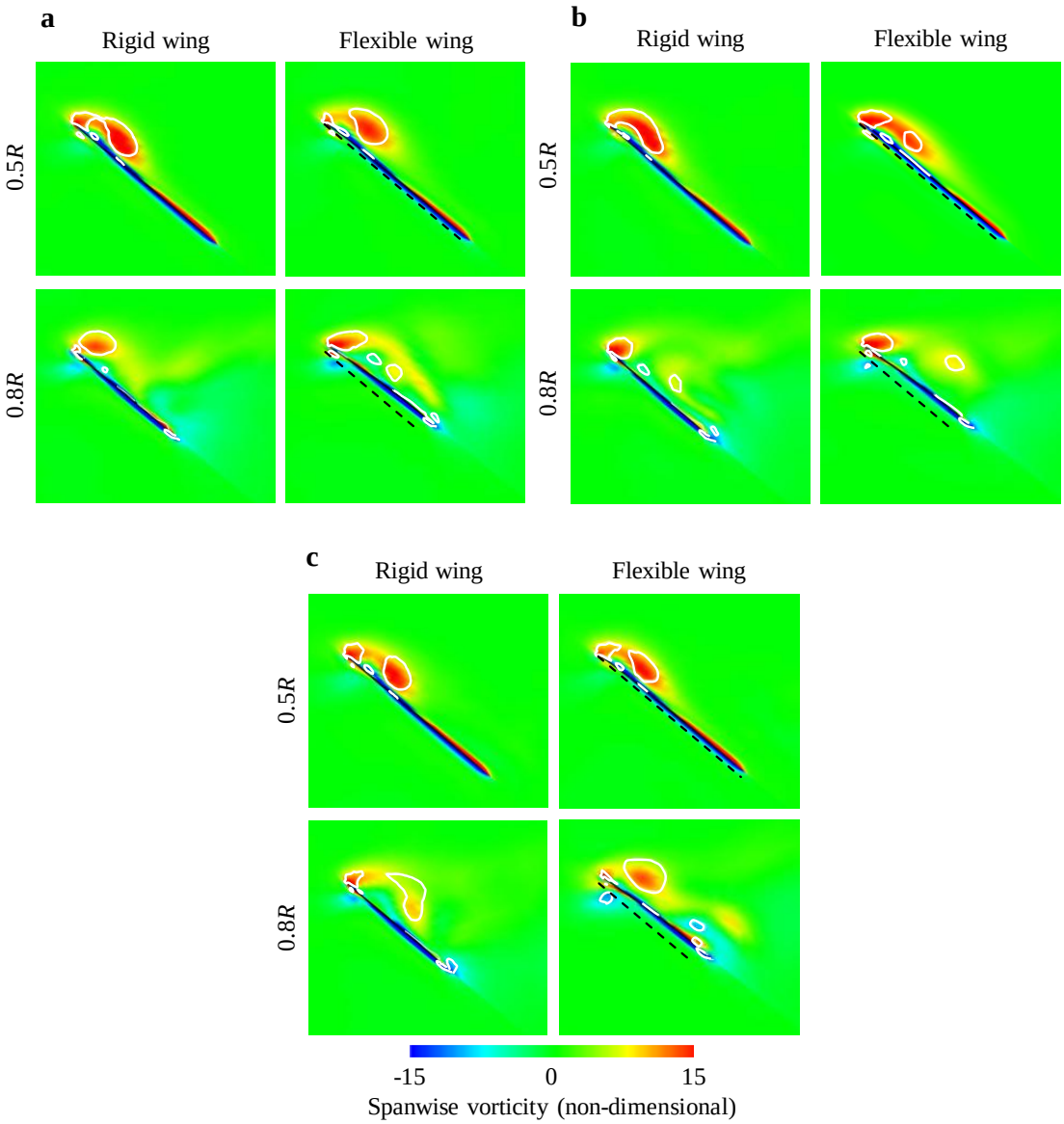

Fig. 2.11 Spanwise vorticity around rigid and flexible wings at angle of wing revolution of (a) 802; (b) 904 and (c) 997 deg. with AoA of 40 deg. Cross-section of a rigid wing is superimposed in the results of flexible wing by dotted line for comparison. White solid lines represent contours of constant Q criterion.

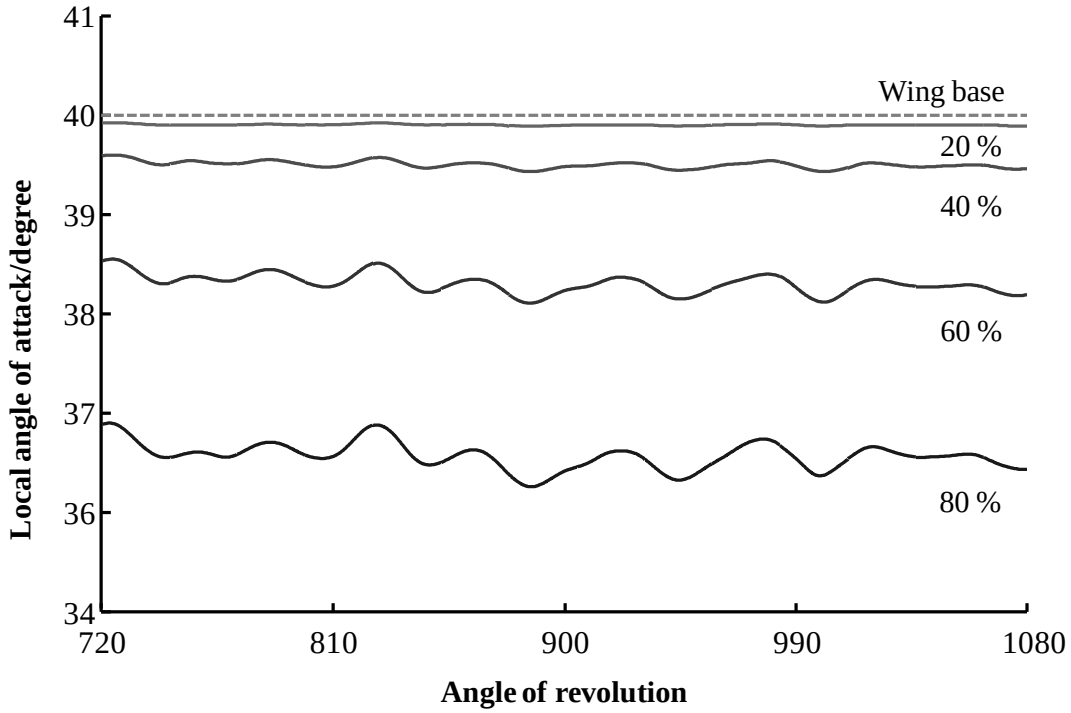

Fig. 2.12 Time courses of local angles of attack of a flexible wing from wing base to tip during steady phase at AoA of 40 deg.

Table 2.1 Force coefficients during unsteady phase at four angles of attack

Angle of attack (degree)	C_v		C_h		C_v/C_h	
	Flexible	Rigid	Flexible	Rigid	Flexible	Rigid
10	0.46	0.50	0.10	0.12	4.46	4.08
20	0.95	0.98	0.32	0.38	2.93	2.60
40	1.62	1.56	1.12	1.22	1.47	1.29
60	1.59	1.44	2.10	2.15	0.77	0.67

Table 2.2 Force coefficients during steady phase at four angles of attack

Angle of attack (degree)	C_v		C_h		C_v/C_h	
	Flexible	Rigid	Flexible	Rigid	Flexible	Rigid
10	0.26	0.28	0.075	0.08	3.38	3.28
20	0.71	0.71	0.25	0.29	2.80	2.45
40	1.27	1.24	0.88	0.96	1.45	1.30
60	1.11	1.01	1.48	1.51	0.75	0.68

Reference

Aono, H., Liu, H. : Vortical structure and aerodynamics of hawkmoth hovering. J. Biomech. Sci. Eng., vol. 1, pp. 234-245 (2006)

Bathe, K. J., Ramm, E., Wilson, E. L.: Finite element formulation for large deformation dynamic analysis. Int. J. Numer. Meth. Eng., vol. 9, pp. 353-386 (1975)

Combes, S. A., Daniel, T. L.: Into thin air: contributions of aerodynamic and inertial-elastic forces to wing bending in the hawkmoth Manduca sexta. J. Exp. Bio., vol. 206, pp. 2999-3006 (2003)

Dickinson, M. H., Lehmann, F.-O. and Sane, S. P.: Wing rotation and the aerodynamic basis of insect flight. Science, vol. 284, pp. 1954-1960 (1999)

Du, G., Sun, M.: Effects of wing deformation on aerodynamic forces in hovering hoverflies. J. Exp. Biol., vol. 213, pp. 2273-2283 (2010)

Ellington, C. P.: The aerodynamics of hovering insect flight. Ⅱ. Morphological parameters. Phil. Trans. R. Soc. Lond. B., vol. 305, pp. 17-40 (1984b)

Ertas, A., Krafcik, J. T., Ekwaro-Osire, S.: Performance of an anisotropic Allman/DKT 3-node thin triangular flat shell element. Compos. Eng., vol. 2, 269 (1992)

Harbig, R. R., Sheridan, J., Thompson, M. C.: Reynolds number and aspect ratio effects on the leading-edge vortex for rotating insect wing planforms. J. Fluid Mech., vol. 717, pp. 166-192 (2013)

Harbig, R. R., Sheridan, J., Thompson, M. C.: Relationship between aerodynamic forces, flow structures and wing camber for rotating insect wing planforms. J. Fluid Mech., vol. 730, pp. 52-75 (2013)

Lentink, D., Dickinson, M. H.: Rotational accelerations stabilize leading edge vortices on revolving fly wings. J. Exp. Biol., vol. 212, pp. 2705-2719 (2009)

Liu, H.: Integrated modeling of insect flight: from morphology, kinematics to aerodynamics. J. Comput. Phys., vol. 228, pp. 439-459 (2009)

Liu, H., Ellington, C. P., Kawachi, K., Van den Berg, C. and Willmott, A.P.: A computational fluid dynamic study of hawkmoth hovering. J. Exp. Biol., vol. 201, pp. 461-477 (1998).

Liu, H., Kawachi, K.: A numerical study of insect flight. J. Comput. Phys., vol. 146, pp. 124-156 (1998)

Mohan, P., Kapania, R. K.: Updated Lagrangian formulation of a flat triangular element for thin laminated shells. AIAA J., vol. 36, pp. 273-281 (1998)

Mountcastle, A. M., Combes, S. A.: Wing flexibility enhances load-lifting capacity in bumblebees. Proc. R. Soc. B., vol. 280 (2013)

Nakata, T., Liu, H.: Aerodynamic performance of a hovering hawkmoth with flexible

wings: a computational approach. Proc. R. Soc. B., vol. 279, pp. 722-731 (2012)

Nakata, T., Liu, H.: A fluid-structure interaction model of insect flight with flexible wings. J. Comput. Phys., vol. 231, pp. 1822-1847 (2012)

Tanaka, H., Whitney, J. P., Wood, R. J.: Effect of flexural and torsional wing flexibility on lift generation in hoverfly flight. Integr. Comp. Biol., vol. 51, 142 (2011)

Usherwood, J. R., Ellington, C. P.: The aerodynamics of revolving wings. Ⅰ. Model hawkmoth wings. J. Exp. Biol., vol. 205, pp. 1547-1564 (2002)

Usherwood, J. R., Ellington, C. P.: The aerodynamics of revolving wings. Ⅱ. Propeller force coefficient from mayfly to quail. J. Exp. Biol., vol. 205, pp. 1565-1576 (2002)

Willmott, A. P., Ellington, C. P.: The mechanism of flight in the hawkmoth Manduca sexta. Ⅰ. kinematics of hovering and forward flight. J. Exp. Bio., vol. 200, pp. 2705-2722 (1997)

Young, J., Walker, S. M., Bomphrey, R. J., Taylor, G. K., Thomas, A. L. R.: Details of insect wing design and deformation enhance aerodynamic function and flight efficiency. Science, vol. 325, pp. 1549-1552 (2009)

Zheng, L., Hedrick, T., Mittal, R.: A comparative study of the hovering efficiency of flapping and revolving wings. Bioinspir. Biomim., vol. 8 (2013)

Zheng, L., Hedrick, T. L., Mittal, R.: Time-varying wing-twist improves aerodynamic efficiency of forward flight in butterflies. PLoS ONE, vol. 8 (2013)

Chapter 3
Flapping wing : Wing deformation of a hovering hawkmoth and aerodynamic performance of the morphing wing

3.1 Introduction

The effect of wing deformation of insects on their flight ability has attracted attentions from researchers in either biology (Combes and Daniel, 2003, Shyy, et al., 2010, Zhao, et al., 2011) or engineering (Tanaka and Shiroyama, 2010, Hinterwirth and Daniel, 2010, Marardika, et al., 2011, Nakata and Liu, 2012) and simultaneous measurement of wing kinematics and deformation for a hovering insect is essential for an integrated understanding of flexible wing aerodynamics and flight maneuvering during flapping flights. However, there are usually some difficulties in filming and recording high-resolution sequences of insect hovering with high-speed video cameras and in digitizing and reconstructing a three-dimensional wing model involving both wing kinematics and deformation with sufficient precision (Zheng, et al., 2013). In this study, aiming at establishing a realistic flapping flexible wing model for hawkmoth hovering, I have developed a method to integrate the digitizing and reconstruction of the wing kinematics and deformations.

3.2 Methods

3.2.1 Animals

Male and female hawkmoths, *Agrius convoluvuli* (Linnaeus, 1758) were obtained in a pupal state from the Research center for advanced science and technology at Tokyo University. Pupae were kept under a 16 hours and 8 hours light:dark cycle at 28 °C. After eclosion, adult moths were kept under a 20 hours and 4 hours light:dark cycle at 27°C for reducing their activity and avoiding damage during flight in the glasshouse. Figure 3.1 show the glasshouse which is designed can control the temperature and maintain the humidity over 80 percent. Note that male and female moths were kept separately because our experimental set-up for measuring of a hovering moth need to induce moths to a certain area by specific fragrance. For maintaining the mass, the adult moths were fed with honey-water (1:10 honey:water) once a day during the activity time. Moreover, the black circle-shaped markers were sprayed on the upper and lower sides of the wings for motion tracking as soon as the adult moth emerge. Note that these painting-mass are less than 8 percent of the total wing mass.

3.2.2 Experimental design for filming of a hovering hawkmoth

After three days from eclosion, the moth's hovering flight were filmed with five high-speed video cameras (Fastcam SA-3, Photron) and four infra red lights as shown in Fig. 3.2. Figure 3.3 also shows the calibration frame with eight metallic spheres used in this study. Note that the dotted background image were given for avoiding the crash to wall and the damage to wings during flight. The resolutions of these high-speed video cameras were 1024×1024 pixels and these were synchronized at 1000 frames per second and set the shutter speed at 1/7500 second. In this study, on the assumption that the wing deformation and wing kinematics are symmetric about the sagittal plane, the right wing was focused for reconstructing a three-dimensional wing model with sufficient precision.

3.2.3 Reconstruction of the wing kinematics and deformation

Figure 3.4 shows the images used in the process of reconstructing the three-dimensional coordinates. Using these continuous images during hovering flight, the markers were tracked and the three-dimensional coordinates were reconstructed with a direct linear transformation (DLT) method. The marker points are consist of four points on the body surface and thirty-four points on the upper and lower sides of wings. Note that these reconstructing process were performed with the application for motion analysis (DIPP-Motion Pro, Ditect).

Using the reconstructed-coordinate points, the wing deformation was reproduced with wing-coordinate. The interpolation of the lacked points which is due to the attitude of a hawkmoth during flight were conducted by least-squares method. In this method, the displacement x_n, y_n at time = t_n was interpolated by real-valued function $f(x, y, t)$ as bellow

$$f(x,y,t) = \sum_{i=1}^{n_i} \sum_{j=1}^{n_j} \sum_{k=1}^{n_k} (a_1(i,j,k)\cos(\frac{k\pi t}{T})x^i y^i + a_2(i,j,k)\sin(\frac{k\pi t}{T})x^i y^i) \quad (3.1)$$

then $a_{1,2}(i,j,k)$ = ($a_{u1,2}(i,j,k)$, $a_{v1,2}(i,j,k)$, $a_{w1,2}(i,j,k)$) was calculated by least-squares method. Moreover, the sum of squares of residual L=(L_u, L_v, L_w) was described as bellow

$$L = \sum_{n=1}^{N} (u_n - f(x_n, y_n, t_n))^2 \quad (3.2)$$

where N denote the all measurement points including the time direction. In this equation, when L get the smallest value the coefficient $a_{1,2}$ (i,j,k) is satisfied with the equation as described bellow

$$\frac{\partial L_u}{\partial a_{u1}(1,1,1)} = 0$$
$$\frac{\partial L_u}{\partial a_{u2}(1,1,1)} = 0 \qquad (3.3)$$
$$\frac{\partial L_u}{\partial a_{u1}(n_i, n_j, n_k)} = 0$$
$$\frac{\partial L_u}{\partial a_{u2}(n_i, n_j, n_k)} = 0$$

the another direction *v*, *w* are described as the same way.

3.3 Results and Discussion

3.3.1 Morphing wing

The initial fore and hind wing model was constructed on the basis of the two-dimensional digitized images, respectively. Then the fore and hind wings were coupled on the basis of the position and holding angle at the wing-base of each wing and treated as the single wing in this study. Figure 3.6 A -B shows the fore and hind wings of a hawkmoth and Fig. 3.6 C-D shows the reconstructed wing models used in this study. The wing length R and mean chord length c_m are 3.60 and 1.24 cm, respectively. Moreover, the reconstructed wing kinematics are shown in Fig. 3.7 and the side view and top view images of reconstructed morphing wing model are also shown in Fig. 3.8. Note that the calculated stroke plane angle is 23 deg, wingbeat amplitude is 101 deg and wingbeat frequency is 39 Hz.

Figure 3.9 B-C show the time courses of feathering angels and camber at each wing span plotted against wingbeat cycles. It is seen that the positive and negative values of feathering angle increase with increasing the position of wing span over the most of the range. Moreover, the all reversal points of feathering angle at each wing span slightly shifts to the end of downstroke. In the time course of the camber, this trend also can be seen, however the positive and negative large values are seen around the middle of the wing span. Considering the difference of the wing size and the scale effect of the stiffness, these wing deformations during a hovering flight have the larger values than that of the computational study by Nakata and Liu (2012) and furthermore, these wing deformations and the trend about the time course are similar to that of the hummingbird (Maeda, 2013).

3.3.2 Aerodynamic performance of the morphing wing

To evaluate the effect of the wing deformation on aerodynamic performance, single wing computation with flat and dynamically morphing wing model was conducted using a biology-inspired numerical flight simulator (Liu, 2009). Grid system for

computational fluid dynamics analysis are shown in Fig. 3.10.

Figure 3.11 A-B show the time courses of the vertical force and power over the third wingbeat cycle and the visualized flow field of the morphing and flat wing model at *t/T* = 2.3 are shown in Fig. 3.12 A-B, respectively. It is seen that the morphing wing model has the lager value than the flat wing model over the most of the range. The peak values of the vertical force and power can be seen around the middle downstroke in both morphing and flat wing models. These trend of the time course are similar to the experimental and computational study (Aono and Liu, 2006, Nakata and Liu 2012, Zheng, et al., 2013). This is due to the development of leading-edge vortex as shown in Fig. 3.12 A-B. Moreover, the strong downwash is seen in the morphing wing model more than the flat wing model because of the existence of the vortex ring which is shaped over the wing base to wing tip in the morphing wing model while the vortex generated around the wing base shed from the wing surface in the flat wing model. Although the wing-body interactions of the flow field are not taken into account in this study, these doubled-time averaged values are sufficient to lift their body.

Using the time-averaged values of the vertical force and power, F_v / P is defined and calculated as the flight efficiency. F_v / P of the morphing wing model is 0.26 and the flat wing model is 0.22. It is revealed that the morphing wing model has the 18 percent higher efficiency compared to that of the flat wing model in this study. These result indicate that the wing deformation enhance the efficiency of the flapping flight as can be seen in the other study (Nakata and Liu, 2012).

3.4 Summary

In this study, aiming at establishing a realistic flapping flexible wing model for hawkmoth hovering, I have developed a method to integrate the digitizing and reconstruction of the wing kinematics and deformations. Male and female hawkmoths, *Agrius convolvuli* are kept separately under the constant light:dark cycle to elicit a stable hovering. After achieving the hovering flight, black circle-shaped markers are applied on the upper and lower sides of the wings as characteristic points. The hovering

flights are recorded with five synchronized high-speed video cameras and four infra red lights. The markers are then tracked and the three-dimensional wing coordinates are reconstructed with a direct linear transformation (DLT) method. Considering the difference of the wing size and the scale effect of the stiffness, the wing deformations of the reconstructed wing model in this study have larger values than that of the past computational studies. Moreover, using a biology-inspired numerical flight simulator, the hawkmoth model with prescribed wing kinematics and deformation are tested. The computational fluid dynamic (CFD) trials for the comparative study of dynamically morphing and flat wing model reveal that the wing deformation enhance not only the aerodynamic force but also the flight efficiency which is defined with the vertical force and power.

Fig. 3.1 Glass house with the thermostat for keeping adult moths.

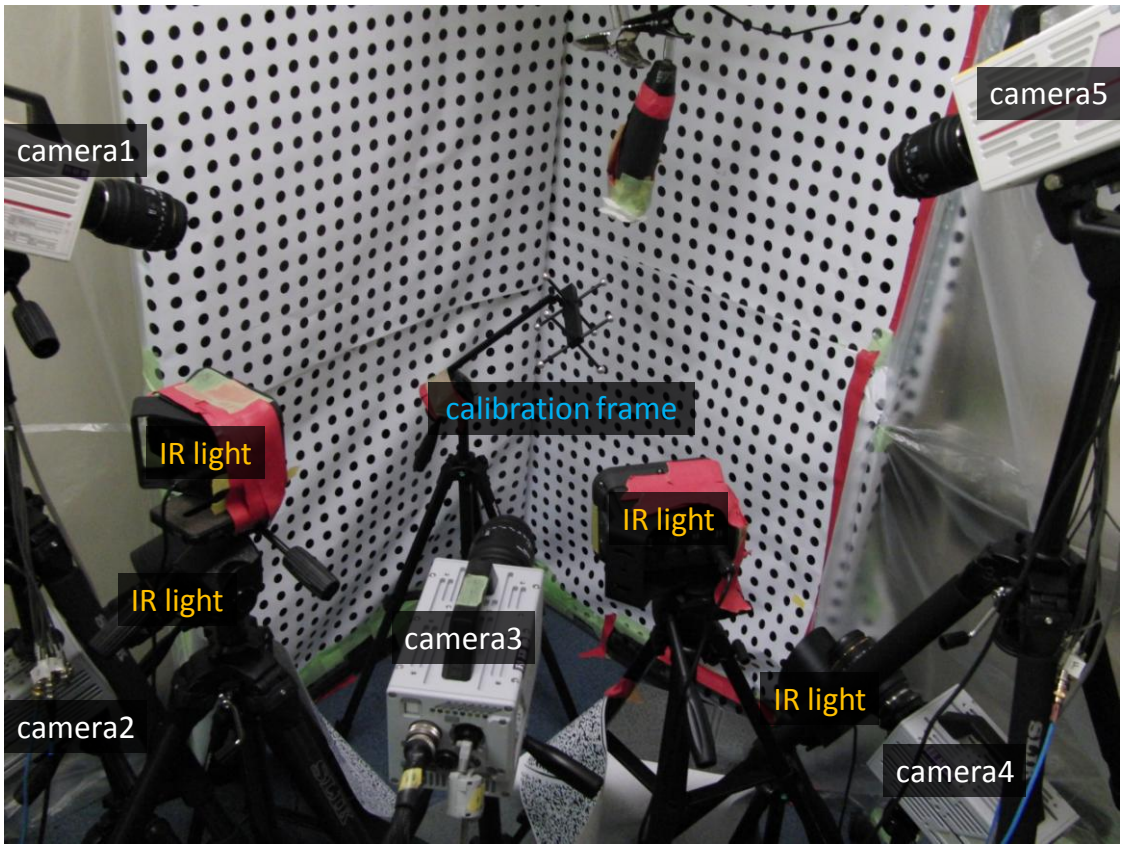

Fig. 3.2 Experimental set-up with five high-speed video cameras and four infra red lights.

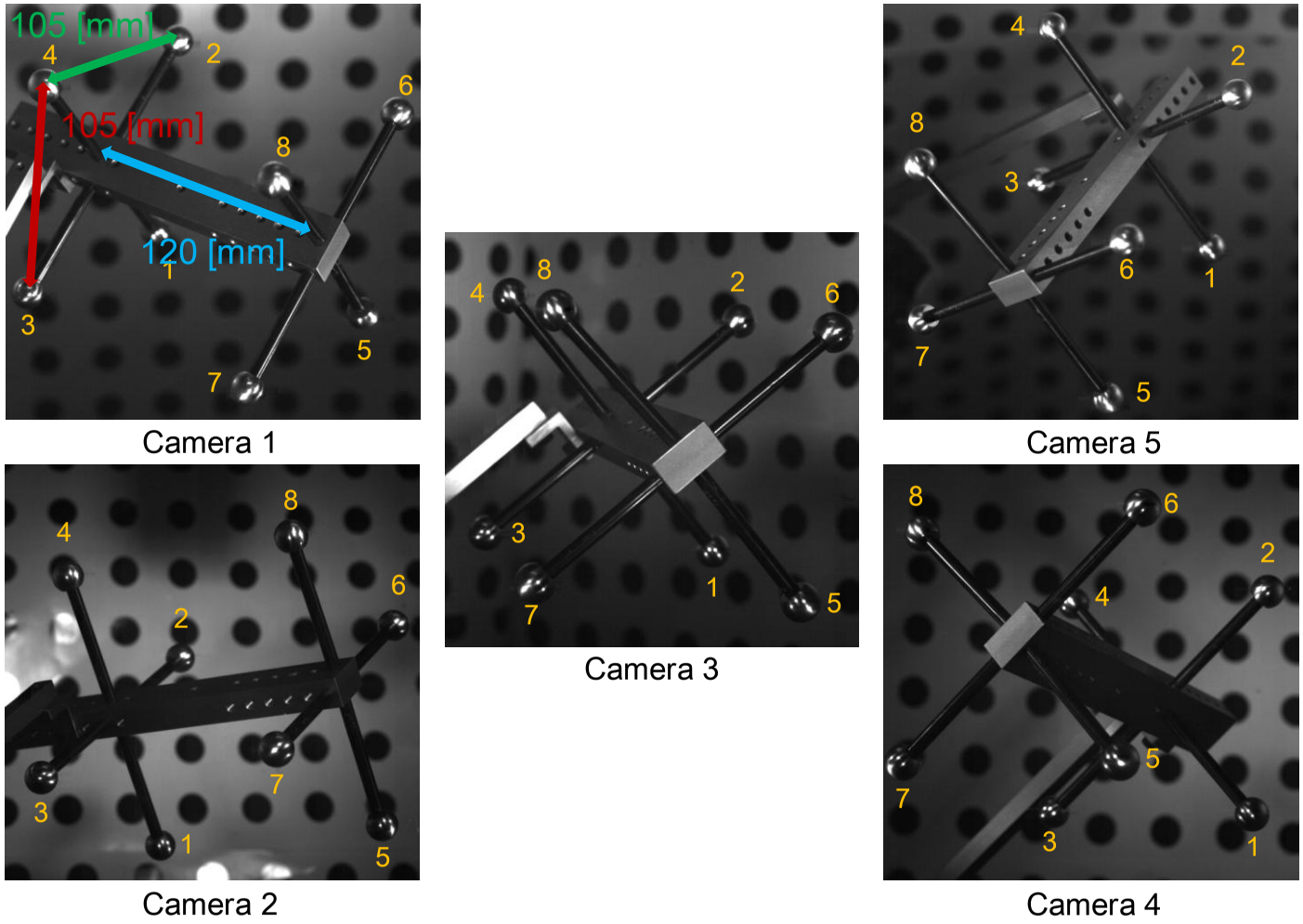

Fig. 3.3 Calibration frame for reconstructing a three-dimensional coordinate.

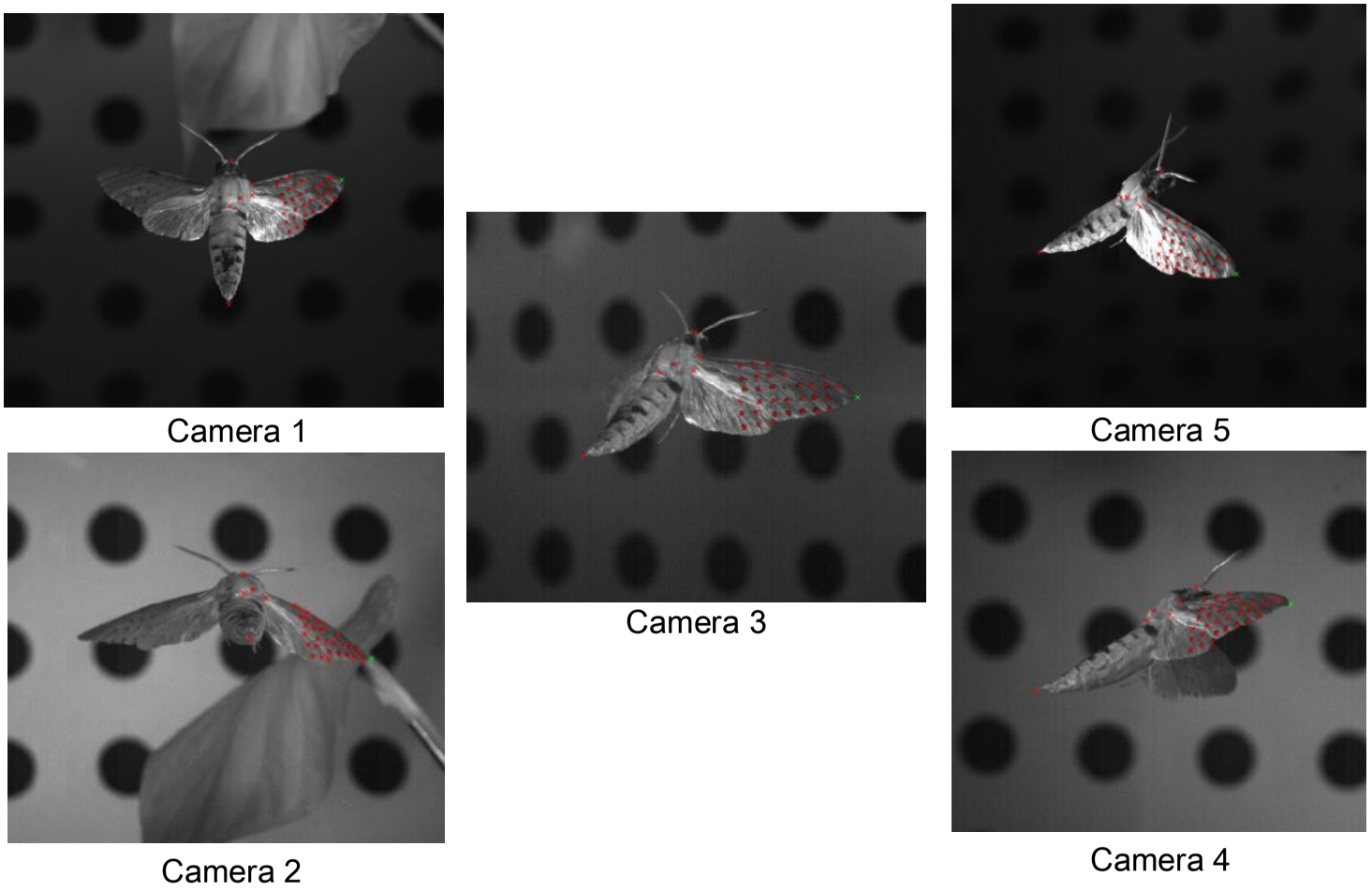

Fig. 3.4 The images of a hovering hawkmoth with circle-shaped markers.

The markers at wing tip are colored by green and the others are colored by red.

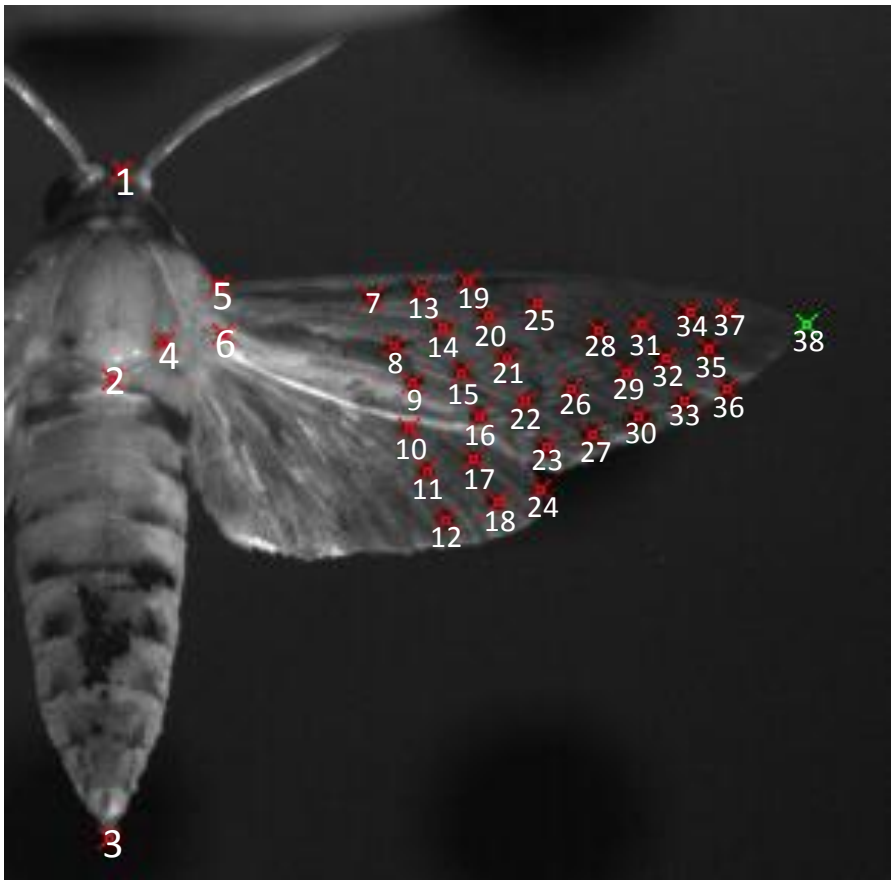

Fig. 3.5 Tracking points for the motion analysis. Four points are applied on the body surface and thirty-four points are applied on the upper and lower sides of the right wing.

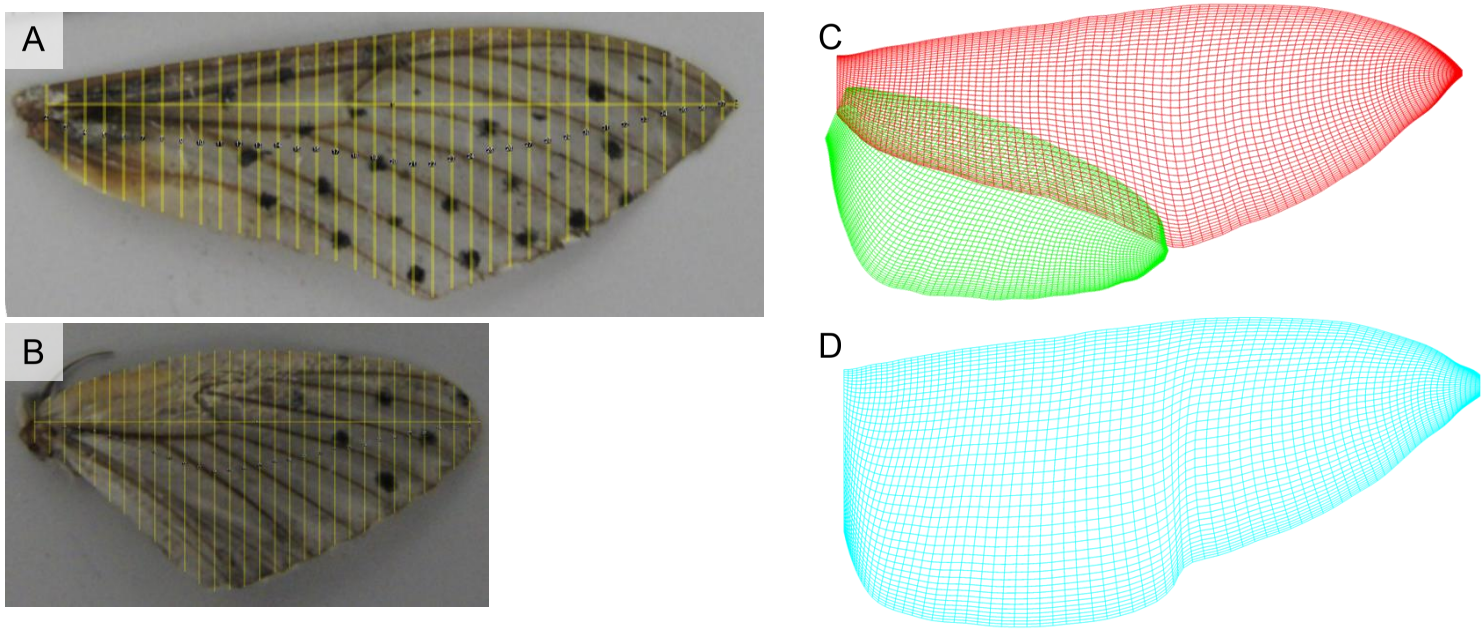

Fig. 3.6 (A) The fore and (B) hind wings of a hawkmoth. (C) The reconstructed fore and hind wing models and (D) single wing model.

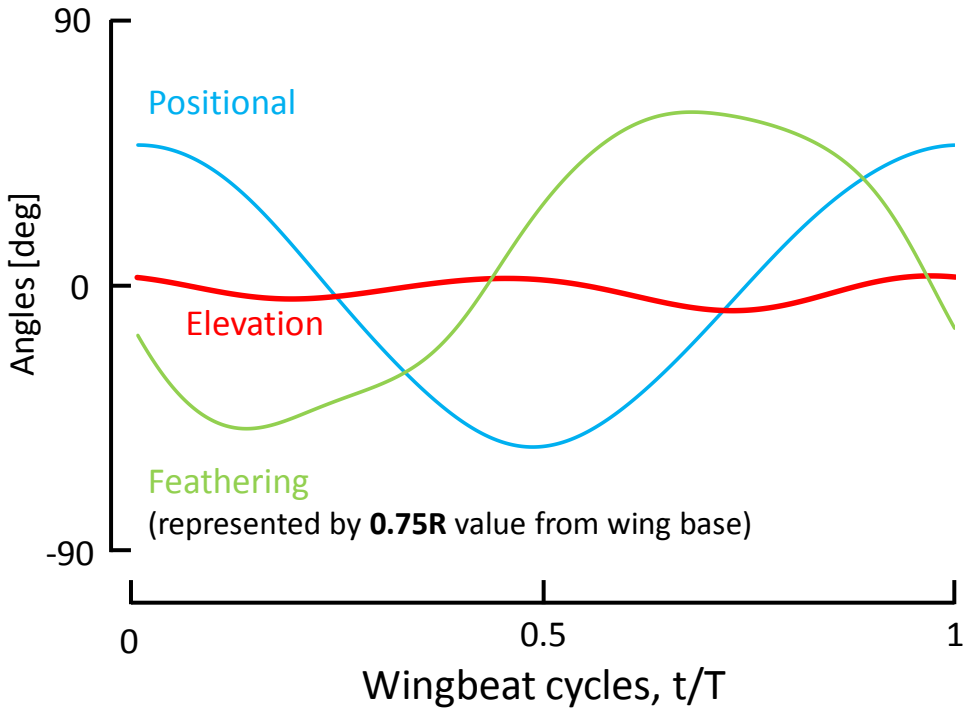

Fig. 3.7 Reconstructed wing kinematics.

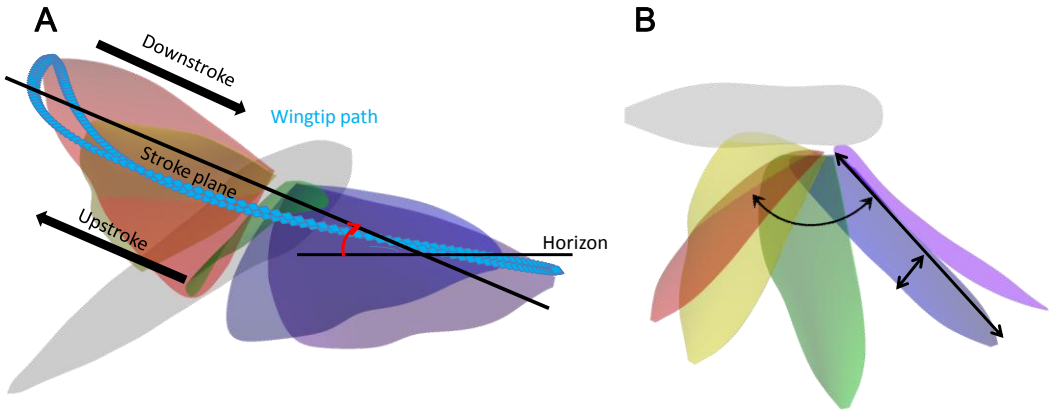

Fig. 3.8 Morphing wing model. (A) Side view and (B) Top view.

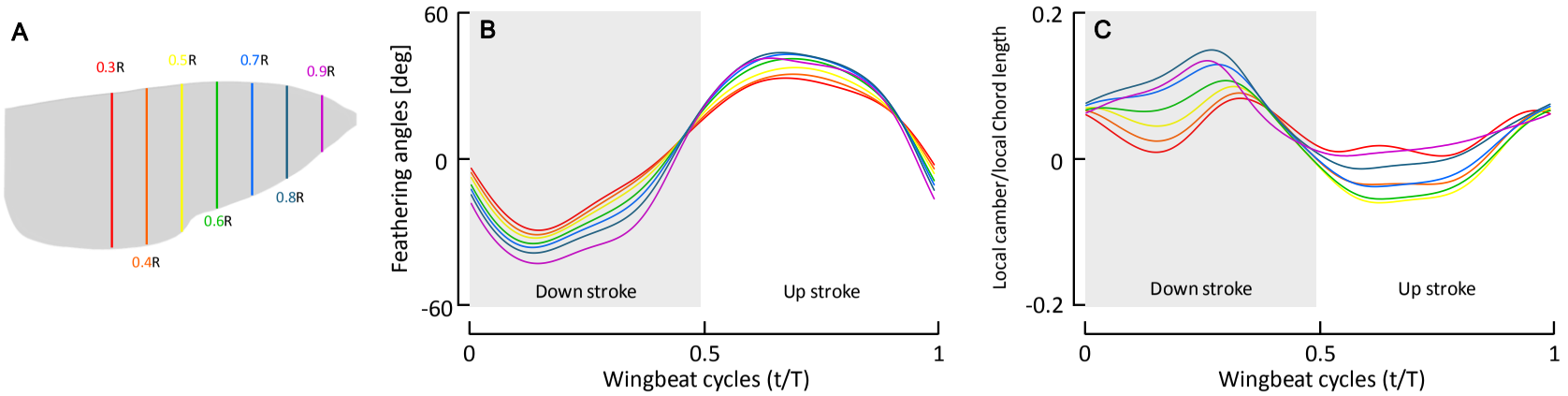

Fig. 3.9 (A) A hawkmoth wing model with colors at each wing span. (B) Time courses of feathering angle and (B) local camber at each wing span. Note that the line colors in (B) and (C) correspond with that in (A).

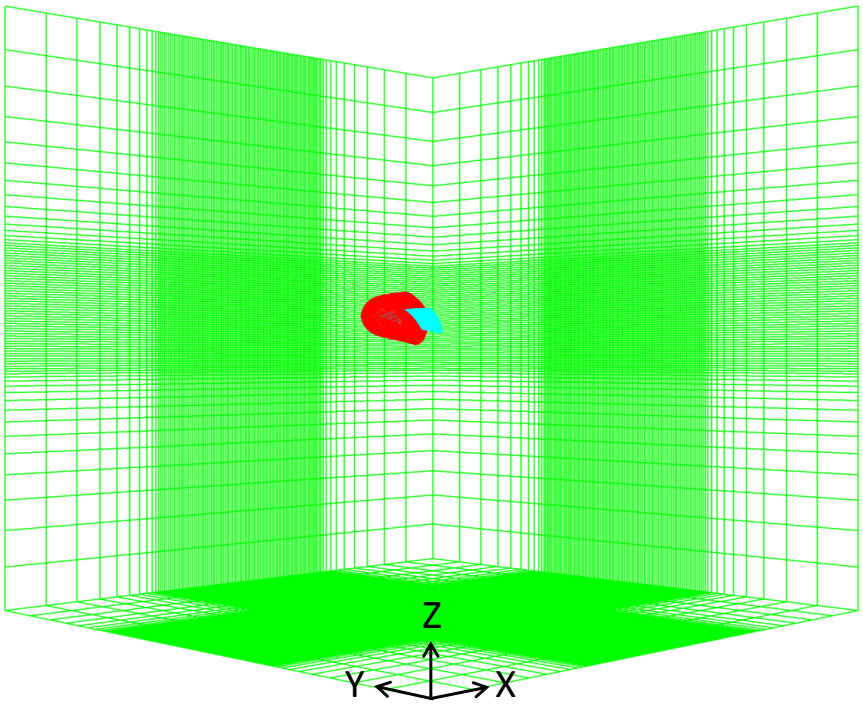

Fig. 3.10 Global and local grids for Computational fluid dynamics analysis..

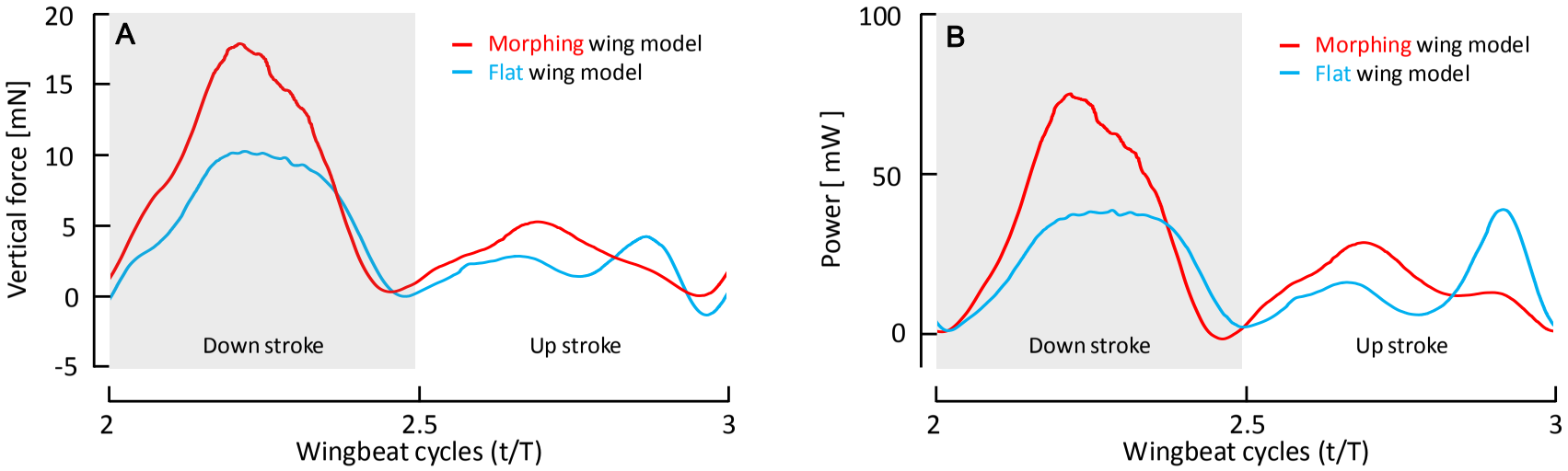

Fig. 3.11 Time courses of (A) the vertical force and (B) power. Note that these result are given from the single-flapping wing computation.

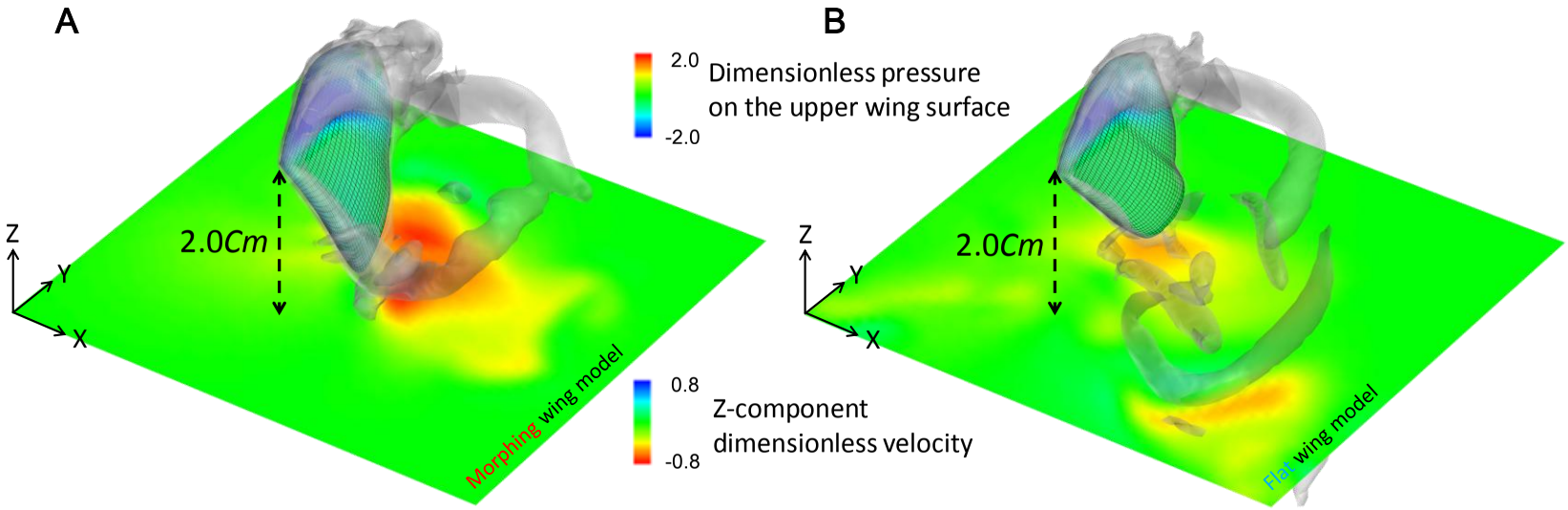

Fig. 3..12 Visualized flow fields of (A) the morphing and (B) flat wing model at *t/T* = 2.3. Gray, smoke-like objects are the iso-surfaces of Q-criterion at 3 and XY-plane are placed at the height of 2.0 mean chord length bellow the wing base pivot for visualization of the Z-component dimensionless velocity.

Reference

Combes, S. A. and Daniel, T. L., Into thin air: contributions of aerodynamic and inertial-elastic forces to wing bending in the hawkmoth Manduca sexta, J. Exp. Biol., vol. 206, pp. 2999-3006 (2003)

Hinterwirth, A. J. and Daniel, T. L., Antennae in the hawkmoth Manduca sexta (Lepidoptera, Sphingidae) mediate abdominal flexion in response to mechanical stimuli, J. Comp. Physiol. A, vol. 196, pp. 947-956 (2010)

Maeda, M., Aerodynamics of Flapping Flight Interacting with Environments, Chiba University PhD thesis (2013)

Mahardika, N., Viet, N. Q. and Park, H. C., Effect of outer wing separation on lift and thrust generation in a flapping wing, Bioinsp. Biomim., vol. 6, pp. 036006 (2011)

Nakata, T. and Liu, H., Aerodynamic performance of a hovering hawkmoth with flexible wings: a computational approach, Proc. R. Soc. B, vol. 279, pp. 722-731 (2012)

Nakata, T. and Liu, H., A fluid-structure interaction model of insect flight with flexible wings. J. Comput. Phys., vol. 231, pp. 1822-1847 (2012)

Shyy, W., Aono, H., Chimakurthi, S. K., Trizila, P., Kang, C.-K., Cesnik, C. E. S. and Liu, H., Recent progress in flapping wing aerodynamics and aeroelasticity, Prog. Aerospace Sci., vol. 46, pp. 284-327 (2010)

Tanaka, H. and Shimoyama, I., Forward flight of swallowtail butterfly with simple flapping motion, Bioinsp. Biomim., vol. 5, pp. 026003 (2010)

Zhao, L., Deng, X. and Sane, S. P., Modulation of leading edge vorticity and aerodynamic forces in flexible flapping wings, Bioinsp. Biomim., vol. 6, pp. 036007 (2011).

Zheng, L., Hedrock, T. L. and Mittal, R., A multi-fidelity modelling approach for evaluation and optimization of wing stroke aerodynamics in flapping flight, J. Fluid Mech., vol. 721, pp. 118-154 (2013)

Chapter 4
Flight dynamics : Effect of the body flexibility with active and passive body models

4.1 Introduction

Insect flight has been attracting attentions from researchers who wish to develop novel bio-inspired micro air vehicles (MAV). Their smart maneuver is, in general, achieved by controlling aerodynamic forces with flapping wings in response to the sensory inputs (Taylor, 2001). In order to understand the flight dynamics and the mechanics of the control, various studies with theoretical or numerical models have been undertaken (Frye, 2001, Hedrick and Daniel, 2006, Sun, et al., 2007, Wu, et al., 2009), which suggest some difficulties in the attitude control of flapping wing flyers. For example, Sun, et al. (2007) reported that there is the inherent instability in pitch direction and suggested that active neural feedback is required for pitch stabilization.

It is also known that insects can change their postures in longitudinal and lateral directions through a joint between thorax and abdomen (Camhi, 1970, Kammer, 1971, Götz, et al., 1979, Zhanker, 1988, Baader, 1990, Fry, et al., 2003, Hinterwirth and Daniel, 2010, Luu, et al., 2011, Dyhr et al., 2013). For example, the abdominal responses of a hawkmoth, *Manduca sexta*, under visual stimuli are observed in pitch direction more than yaw or roll direction (Hinterwirth and Daniel, 2010, Dyhr et al., 2013). Even though the body flexion looks small, it can affect the flight dynamics and stabilities (Yokoyama, et al., 2013, Kim and Han, 2014). In order to understand the

flight dynamics of insects with the body flexion and to find novel control strategies for MAV, I investigate the effect of the longitudinal active and passive body flexion on flight dynamics by using an *in-house* CFD and FBD solver. The active body flexion is assumed to be static flexion of the body, and the kinematics model is constructed on the basis of the observations (Dyhr et al., 2013). The passive body models that have the flexibility in a joint between thorax and abdomen are also constructed with a three-dimensional flexible beam model. Based on the simulated results, I further discuss on the flight control and stability of the flyers with the active and passive abdominal flexion in terms of the design of flapping-winged MAVs.

4.2 Methods

4.2.1 Morphological and kinematic models of a hovering hawkmoth

In this study, I use the morphological model of a hawkmoth, *Agrius convolvuli*, that was originally developed by Aono and Liu (2006) on the basis of the two-dimensional digitized image. The realistic kinematic model of a hovering hawkmoth is based on the measurement of the hawkmoth *Manduca sexta*, by Willmott and Ellington (1997). Note that wing kinematics model is constructed with the Fourier series as the same way in Liu, et al. (1998a). Figure 4.1A and B show the definitions of three-dimensional movement of a flapping wing and the time-series data of each angle for flapping wing. The major parameter used in this study, including the parameter used for an *in-house* CFD and a FBD solver are also shown in Table 4.1.

4.2.2 Flexible body dynamics solver

Finite element method (FEM), which is often used for formularization of beam with large deformation and large rotation, includes floating reference frame method, incremental finite element method, large rotational vector method, absolute nodal method, and so forth. In this study, update reference frame method which was one of the floating reference frame method, was employed to formularize the equations. Force of

each element and tangent modulus matrix are derived through infinitesimal deformation theory based on coordinates of the element just before updated due to motion of the beam. Equations of motion in update reference frame method are

$$\mathbf{M}\ddot{\mathbf{q}} + \mathbf{C}\dot{\mathbf{q}} + \mathbf{K}_{\mathbf{L}}\mathbf{q} + \mathbf{f}_{\mathbf{int}}(\mathbf{q}) - \mathbf{f}_{\mathbf{ext}} = 0 \tag{4.1}$$

where **M**, **C** and $\mathbf{K}_{\mathbf{L}}$ are mass, damping, and stiffness matrices, respectively. $\mathbf{f}_{\text{ext}}$ is external force. $\mathbf{f}_{\text{int}}(\mathbf{q})$, which is restoring force occurring with deformation of the beam, is a nonlinear function of the generalized coordinate **q.** Tangent modulus matrix $\mathbf{K}_{\mathbf{N}}$ is also required for numerical integration.

$$\mathbf{K}_{\mathbf{N}} = \partial \mathbf{f}_{\mathbf{int}} / \partial \mathbf{q} \tag{4.2}$$

Internal stress and stiffness matrix in this method are as follows. Orthogonal reference frame *O-XYZ* and element reference frame *o-xyz*, which is defined at each position of the element, are employed as coordinate systems (Fig. 4.2). Here I named the state just before present one and present state as "preceding state" and "current state", respectively. They show the context not only in time but also in Newton iterative process. In element reference frame, *z*-axis is oriented from node *i* to *j*, and *x*, *y*-axes are then determined so as to be perpendicular to *z*-axis. Both reference frames are right-handed coordinate systems and *x*, *y*-axes are oriented toward the principal axis of each cross-section. Displacement of certain node *i* in the generalized coordinate system in terms of orthogonal reference frame $\mathbf{q}_{\mathbf{i}}$ and element reference frame $\mathbf{q}'_{\mathbf{i}}$ can be expressed as:

$$\mathbf{q_i} = \begin{bmatrix} x_i \\ y_i \\ z_i \\ \Phi_i \\ \Theta_i \\ \Psi_i \end{bmatrix} \qquad \mathbf{q'_i} = \begin{bmatrix} u_i \\ v_i \\ w_i \\ \varphi_i \\ \theta_i \\ \psi_i \end{bmatrix} \tag{4.3}$$

where subscript *i, j* denote numbers of nodes at both ends of the beam. Considering the preceding and current state at the beam element *i-j*, increment of displacement $\Delta\mathbf{q}$ can be calculated as:

$$\Delta\mathbf{q} = \mathbf{q} - \mathbf{q_b} \tag{4.4}$$

where $\mathbf{q_b}$ is the generalized coordinate of both ends of the beam in preceding state, $\mathbf{q}$ that in current state. By expressing Eq. (4.4) in the element reference frame, following equation is derived:

$$\Delta\mathbf{q}' = \mathbf{T_b}\Delta\mathbf{q} \tag{4.5}$$

where $\mathbf{T}_b$ is transformation matrix which has 12×12 elements: includes four 3×3 matrices $\mathbf{\Lambda}_b$, which transform the coordinate from orthogonal to element reference frame, as diagonal components. With the components of node *i, j* at both ends of the element, $\Delta\mathbf{q}$' can be expressed as:

$$\Delta\mathbf{q}' = \begin{bmatrix} \Delta u_i & \Delta v_i & \Delta w_i & \Delta\varphi_i & \Delta\theta_i & \Delta\psi_i & \Delta u_j & \Delta v_j & \Delta w_j & \Delta\varphi_j & \Delta\theta_j & \Delta\psi_j \end{bmatrix}^T \tag{4.6}$$

The angles between *z*, *y* and *x*-axes in preceding state and those in current state shown in Fig. 4.3, namely increment of beam attitude angle, can be defined as:

$$\hat{\Delta}u = \frac{\Delta u_j - \Delta u_i}{l_b}, \quad \hat{\Delta}v = \frac{\Delta v_j - \Delta v_i}{l_b}, \quad \hat{\Delta}w = \frac{\Delta w_j - \Delta w_i}{l_b} \tag{4.7}$$

With Eqs. (4.6) and (4.7), increment of angular deformation can be calculated as:

$$\begin{aligned}\Delta\boldsymbol{\varepsilon}_{\mathbf{i}} &\equiv \begin{bmatrix}\Delta\varepsilon_{xi}\\ \Delta\varepsilon_{yi}\\ \Delta\varepsilon_{zi}\end{bmatrix}\\ &= \frac{1}{4}\begin{bmatrix} 4(\hat{\Delta}v - \hat{\Delta}v\hat{\Delta}w - \Delta\psi_i\hat{\Delta}u + \Delta\phi_i) + 2\Delta\theta_i\Delta\psi_i - (\Delta\psi_j - \Delta\psi_i)(\hat{\Delta}u - \Delta\theta_i)\\ 4(-\hat{\Delta}u + \hat{\Delta}u\hat{\Delta}w - \Delta\psi_i\hat{\Delta}v + \Delta\theta_i) - 2\Delta\phi_i\Delta\psi_i - (\Delta\psi_j - \Delta\psi_i)(\hat{\Delta}v + \Delta\phi_i)\\ -2(\Delta\psi_j - \Delta\psi_i) - \hat{\Delta}v(\Delta\theta_j - \Delta\theta_i) - \hat{\Delta}u(\Delta\phi_j - \Delta\phi_i)\end{bmatrix}\\ &\cong \begin{bmatrix}\hat{\Delta}v + \Delta\phi_i\\ -\hat{\Delta}u + \Delta\theta_i\\ -(\Delta\psi_j - \Delta\psi_i)/2\end{bmatrix}\end{aligned} \tag{4.8}$$

$$\begin{aligned}\Delta\boldsymbol{\varepsilon}_{\mathbf{j}} &\equiv \begin{bmatrix}\Delta\varepsilon_{xj}\\ \Delta\varepsilon_{yj}\\ \Delta\varepsilon_{zj}\end{bmatrix}\\ &= \frac{1}{4}\begin{bmatrix} 4(\hat{\Delta}v - \hat{\Delta}v\hat{\Delta}w - \Delta\psi_j\hat{\Delta}u + \Delta\phi_j) + 2\Delta\theta_j\Delta\psi_j - (\Delta\psi_i - \Delta\psi_j)(\hat{\Delta}u - \Delta\theta_j)\\ 4(-\hat{\Delta}u + \hat{\Delta}u\hat{\Delta}w - \Delta\psi_j\hat{\Delta}v + \Delta\theta_j) - 2\Delta\phi_j\Delta\psi_j - (\Delta\psi_i - \Delta\psi_j)(\hat{\Delta}v + \Delta\phi_j)\\ -2(\Delta\psi_i - \Delta\psi_j) - \hat{\Delta}v(\Delta\theta_i - \Delta\theta_j) - \hat{\Delta}u(\Delta\phi_i - \Delta\phi_j)\end{bmatrix}\\ &\cong \begin{bmatrix}\hat{\Delta}v + \Delta\phi_j\\ -\hat{\Delta}u + \Delta\theta_j\\ -(\Delta\psi_i - \Delta\psi_j)/2\end{bmatrix}\end{aligned} \tag{4.9}$$

where the last term, which is the approximation derived by neglecting second-order infinitesimal, is described for intuitive comprehension. For example, $\Delta\varepsilon_{yi}$ denotes increment of angular deformation around y-axis at node *i*; it is derived by subtracting increment of attitude angle from that of angular displacement. Deformation of the current state $\boldsymbol{\varepsilon}$ is

$$\boldsymbol{\varepsilon} = \boldsymbol{\varepsilon}_b + \Delta\boldsymbol{\varepsilon} \tag{4.10}$$

given that

$$\boldsymbol{\varepsilon} = \begin{bmatrix} \varepsilon_{xi} & \varepsilon_{yi} & \varepsilon_{zi} & \varepsilon_{xj} & \varepsilon_{yj} & \varepsilon_{zj} \end{bmatrix}^T$$

$$\Delta\boldsymbol{\varepsilon} = \begin{bmatrix} \Delta\varepsilon_{xi} & \Delta\varepsilon_{yi} & \Delta\varepsilon_{zi} & \Delta\varepsilon_{xj} & \Delta\varepsilon_{yj} & \Delta\varepsilon_{zj} \end{bmatrix}^T$$

where $\boldsymbol{\varepsilon}$ and $\Delta\boldsymbol{\varepsilon}$ are angular displacement and its increment, respectively. Axial elongation ε_L is derived by subtracting natural length l_0 from current length l, which is calculated with **q:**

$$\varepsilon_L = l - l_0$$

Therefore force of element in current state $\mathbf{f'_{int}}$ is described as:

$$\mathbf{f'_{int}} = \begin{bmatrix} f'_{xi} & f'_{y_i} & f'_{zi} & M'_{xi} & M'_{y_i} & M'_{zi} & f'_{x\,j} & f'_{y\,j} & f'_{z\,j} & M'_{x\,j} & M'_{y\,j} & M'_{z\,j} \end{bmatrix}^T$$

where

$$f'_{xi} = \frac{6EI_y}{l^2}\left(\varepsilon_{yi} + \varepsilon_{yj}\right) \qquad f'_{xj} = -f'_{xi}$$

$$f'_{yi} = -\frac{6EI_x}{l^2}\left(\varepsilon_{xi} + \varepsilon_{xj}\right) \qquad f'_{yj} = -f'_{yi}$$

$$f'_{zi} = -\frac{EA}{l}\varepsilon_L \qquad f'_{zj} = -f'_{zi}$$

$$M'_{xi} = \frac{2EI_x}{l}\left(2\varepsilon_{xi} + \varepsilon_{xj}\right) \qquad M'_{xj} = \frac{2EI_x}{l}\left(\varepsilon_{xi} + 2\varepsilon_{xj}\right)$$

$$M'_{yi} = \frac{2EI_y}{l}\left(2\varepsilon_{yi} + \varepsilon_{yj}\right) \qquad M'_{yj} = \frac{2EI_y}{l}\left(\varepsilon_{yj} + 2\varepsilon_{yj}\right)$$

$$M'_{zi} = -\frac{GJ}{l}\left(\varepsilon_{zj} - \varepsilon_{zi}\right) \qquad M'_{zj} = -M_{zi}$$

By transforming coordinate of $\mathbf{f'_{int}}$ with transformation matrix in current state **T,** force of element in orthogonal reference frame $\mathbf{f_{int}}$ is gained as:

$$\mathbf{f_{int}} = \mathbf{T^T f'_{int}} \tag{4.11}$$

On the other hand, stiffness matrix consists of elastic deformation matrix $\mathbf{K'}_0$ and geometric stiffness matrix $\mathbf{K'}_G$. These matrices are expressed as:

$$\mathbf{K}_0' = \begin{bmatrix}
\frac{12EI_y}{l^3} & 0 & 0 & 0 & \frac{6EI_y}{l^2} & 0 & -\frac{12EI_y}{l^3} & 0 & 0 & 0 & \frac{6EI_y}{l^2} & 0 \\
0 & \frac{12EI_x}{l^3} & 0 & -\frac{6EI_x}{l^2} & 0 & 0 & 0 & -\frac{12EI_x}{l^3} & 0 & -\frac{6EI_x}{l^2} & 0 & 0 \\
0 & 0 & \frac{EA}{l} & 0 & 0 & 0 & 0 & 0 & -\frac{EA}{l} & 0 & 0 & 0 \\
0 & -\frac{6EI_x}{l^2} & 0 & \frac{4EI_x}{l} & 0 & 0 & 0 & \frac{6EI_x}{l^2} & 0 & \frac{2EI_x}{l} & 0 & 0 \\
\frac{6EI_y}{l^2} & 0 & 0 & 0 & \frac{4EI_y}{l} & 0 & -\frac{6EI_y}{l^2} & 0 & 0 & 0 & \frac{2EI_y}{l} & 0 \\
0 & 0 & 0 & 0 & 0 & \frac{GI_p}{l} & 0 & 0 & 0 & 0 & 0 & -\frac{GI_p}{l} \\
-\frac{12EI_y}{l^3} & 0 & 0 & 0 & -\frac{6EI_y}{l^2} & 0 & \frac{12EI_y}{l^3} & 0 & 0 & 0 & -\frac{6EI_y}{l^2} & 0 \\
0 & -\frac{12EI_x}{l^3} & 0 & \frac{6EI_x}{l^2} & 0 & 0 & 0 & \frac{12EI_x}{l^3} & 0 & \frac{6EI_x}{l^2} & 0 & 0 \\
0 & 0 & -\frac{EA}{l} & 0 & 0 & 0 & 0 & 0 & \frac{EA}{l} & 0 & 0 & 0 \\
0 & -\frac{6EI_x}{l^2} & 0 & \frac{2EI_x}{l} & 0 & 0 & 0 & \frac{6EI_x}{l^2} & 0 & \frac{4EI_x}{l} & 0 & 0 \\
\frac{6EI_y}{l^2} & 0 & 0 & 0 & \frac{2EI_y}{l} & 0 & -\frac{6EI_y}{l^2} & 0 & 0 & 0 & \frac{4EI_y}{l} & 0 \\
0 & 0 & 0 & 0 & 0 & -\frac{GI_p}{l} & 0 & 0 & 0 & 0 & 0 & \frac{GI_p}{l}
\end{bmatrix}$$

$$\mathbf{K}_G' = \begin{bmatrix}
\frac{T}{l} & 0 & \frac{V}{l} & \frac{M_T}{2l} & 0 & \overline{W}_{xi} & -\frac{T}{l} & 0 & \frac{V}{l} & -\frac{M_T}{2l} & 0 & \overline{W}_{xj} \\
0 & \frac{T}{l} & \frac{W}{l} & 0 & \frac{M_T}{2l} & \overline{V}_{xi} & 0 & -\frac{T}{l} & -\frac{W}{l} & 0 & -\frac{M_T}{2l} & \overline{V}_{xi} \\
\frac{V}{l} & \frac{W}{l} & 0 & 0 & 0 & 0 & -\frac{V}{l} & -\frac{W}{l} & 0 & 0 & 0 & 0 \\
\frac{M_T}{2l} & 0 & 0 & 0 & 0 & -\frac{M_{yi}}{4} & -\frac{M_T}{2l} & 0 & 0 & 0 & 0 & -\frac{M_{yi}}{4} \\
0 & \frac{M_T}{2l} & 0 & 0 & 0 & \frac{M_{xi}}{4} & 0 & -\frac{M_T}{2l} & 0 & 0 & 0 & \frac{M_{xi}}{4} \\
\overline{W}_{xi} & \overline{V}_{xi} & 0 & -\frac{M_{yi}}{4} & \frac{M_{xi}}{4} & 0 & -\overline{W}_{xi} & -\overline{V}_{xi} & 0 & -\frac{M_{yj}}{4} & -\frac{M_{xj}}{4} & 0 \\
-\frac{T}{l} & 0 & -\frac{V}{l} & -\frac{M_T}{2l} & 0 & -\overline{W}_{xi} & \frac{T}{l} & 0 & \frac{V}{l} & \frac{M_T}{2l} & 0 & -\overline{W}_{xj} \\
0 & -\frac{T}{l} & -\frac{W}{l} & 0 & -\frac{M_T}{2l} & -\overline{V}_{xi} & 0 & \frac{T}{l} & \frac{W}{l} & 0 & \frac{M_T}{2l} & -\overline{V}_{xj} \\
-\frac{V}{l} & -\frac{W}{l} & 0 & 0 & 0 & 0 & \frac{V}{l} & \frac{W}{l} & 0 & 0 & 0 & 0 \\
-\frac{M_T}{2l} & 0 & 0 & 0 & 0 & -\frac{M_{yj}}{4} & \frac{M_T}{2l} & 0 & 0 & 0 & 0 & -\frac{M_{yj}}{4} \\
0 & -\frac{M_T}{2l} & 0 & 0 & 0 & -\frac{M_{xj}}{4} & 0 & \frac{M_T}{2l} & 0 & 0 & 0 & \frac{M_{xj}}{4} \\
\overline{W}_{xj} & \overline{V}_{xj} & 0 & -\frac{M_{yi}}{4} & \frac{M_{xi}}{4} & 0 & -\overline{W}_{xj} & -\overline{V}_{xj} & 0 & -\frac{M_{yj}}{4} & \frac{M_{xj}}{4} & 0
\end{bmatrix}$$

where

$$T=(EA/l)\varepsilon_L \qquad M_T=(GJ/l)(\varepsilon_{zj}-\varepsilon_{zi})$$

$$\overline{V}_{xi}=(3M_{yi}+M_{yj})/4l \qquad \overline{V}_{xj}=(M_{yi}+3M_{yj})/4l$$

$$\overline{W}_{xi}=(3M_{xi}+M_{xj})/4l \qquad \overline{W}_{xj}=(M_{xi}+3M_{xj})/4l$$

Stiffness matrix in orthogonal reference frame $\mathbf{K}_{\mathrm{N}}$ is then derived by transforming coordinate, such as:

$$\mathbf{K_N}=\mathbf{T}^{\mathbf{T}}[\mathbf{K_0'}+\mathbf{K_G'}]\mathbf{T} \tag{4.12}$$

Synthesizing $\mathbf{f}_{int}$、$\mathbf{K}_{\mathrm{N}}$ for all the elements of beam, force of element and stiffness matrix for all the degrees of freedom can be calculated. Hence equations of motion can also be constructed. Note that coordinate transformation matrix **T** should be updated based on the preceding state, such that:

$$\mathbf{T}=\mathrm{diag}[\Lambda \quad \Lambda \quad \Lambda \quad \Lambda] \quad \Lambda=\Delta\Lambda\Lambda_{\mathrm{b}} \quad \Delta\Lambda=\mathbf{A}^{\hat{\mathbf{i}}\mathbf{i}''}\mathbf{A}^{\mathbf{i}''\mathbf{i}}$$

where $\mathbf{\Lambda}_b$ is known; $\mathbf{A}^{\mathbf{i}''\mathbf{i}}$, $\mathbf{A}^{\hat{\mathbf{i}}\mathbf{i}''}$**,** components of $\Delta\mathbf{\Lambda}$**,** are derived as:

$$\mathbf{A}^{\mathbf{i}''\mathbf{i}}=\begin{bmatrix} 1-\frac{1}{2}(\hat{\Delta}u^2+\Delta\psi_i{}^2) & -\Delta\psi_i-\frac{1}{2}(\hat{\Delta}u\hat{\Delta}v+\Delta\psi_i\hat{\Delta}u+\Delta\theta_i\hat{\Delta}v) & -\hat{\Delta}u+\hat{\Delta}u\hat{\Delta}w-\Delta\psi_i\hat{\Delta}v \\ -\Delta\psi_i-\frac{1}{2}(\hat{\Delta}u\hat{\Delta}v+\Delta\psi_i\hat{\Delta}u-\Delta\theta_i\hat{\Delta}v) & 1-\frac{1}{2}(\hat{\Delta}v^2+\Delta\psi_i{}^2) & -\hat{\Delta}v+\hat{\Delta}v\hat{\Delta}w+\Delta\psi_i\hat{\Delta}u \\ \hat{\Delta}u-\hat{\Delta}u\hat{\Delta}w & \hat{\Delta}v+\hat{\Delta}u\hat{\Delta}w & 1-\frac{1}{2}(\hat{\Delta}u^2+\hat{\Delta}v^2) \end{bmatrix}$$

$$\mathbf{A}^{\hat{\mathbf{i}}\mathbf{i}''}=\begin{bmatrix} \mathrm{c} & \mathrm{s} & 0 \\ -\mathrm{s} & \mathrm{c} & 0 \\ 0 & 0 & 1 \end{bmatrix}$$

where

$$c=1-\frac{1}{8}(\Delta\psi_j-\Delta\psi_i)^2$$

$$s=\frac{1}{2}(\Delta\psi_j-\Delta\psi_i)+\frac{\hat{\Delta}u}{4}(\Delta\phi_j-\Delta\phi_i)+\frac{\hat{\Delta}v}{4}(\theta_j-\Delta\theta_i)$$

Neglecting high-order infinitesimal term for simplicity and intuitive comprehension, $\Delta\mathbf{\Lambda}$ can be expressed as:

$$\begin{aligned}\Delta\Lambda = \mathbf{A}^{\hat{\mathbf{i}}\mathbf{i}''}\mathbf{A}^{\mathbf{i}''\mathbf{i}} &= \begin{bmatrix} 1 & (\Delta\psi_j - \Delta\psi_i)/2 & 0 \\ -(\Delta\psi_j - \Delta\psi_i)/2 & 1 & 0 \\ 0 & 0 & 1 \end{bmatrix}\begin{bmatrix} 1 & \Delta\psi_i & -\hat{\Delta}u \\ -\Delta\psi_i & 1 & -\hat{\Delta}v \\ \hat{\Delta}u & \hat{\Delta}v & 1 \end{bmatrix} \\ &\cong \begin{bmatrix} 1 & (\Delta\psi_j + \Delta\psi_i)/2 & -\hat{\Delta}u \\ -(\Delta\psi_j + \Delta\psi_i)/2 & 1 & -\hat{\Delta}v \\ -\hat{\Delta}u & \hat{\Delta}v & 1 \end{bmatrix} \\ &\cong \begin{bmatrix} 1 & 0 & 0 \\ 0 & 1 & -\hat{\Delta}v \\ 0 & \hat{\Delta}v & 1 \end{bmatrix}\begin{bmatrix} 1 & 0 & -\hat{\Delta}u \\ 0 & 1 & 0 \\ \hat{\Delta}u & 0 & 1 \end{bmatrix}\begin{bmatrix} 1 & (\Delta\psi_j + \Delta\psi_i)/2 & 0 \\ -(\Delta\psi_j + \Delta\psi_i)/2 & 1 & 0 \\ 0 & 0 & 1 \end{bmatrix}\end{aligned} \tag{4.13}$$

In preceding equations, multiplication of three matrices means the rotation around x_b, y_b and z_b-axis by angles $\hat{\Delta}v$、$\hat{\Delta}u$、$(\Delta\psi_i + \Delta\psi_j)/2$, respectively. For example, Fig. 4.4 shows the schematic description of the beam from z_b-axis direction, where the position at the left end of the beam i in current state is translated so that it overlaps with that in preceding state.

$$\frac{\psi_i + \psi_j}{2} - \frac{\psi_{ib} + \psi_{jb}}{2} = \frac{\Delta\psi_i + \Delta\psi_j}{2} \tag{4.14}$$

In this study, numerical integration was conducted through Newmark-β method and Newton-Raphson method[6]. Approximate solution at t_{n+1} is computed through time integration method assuming displacement, velocity, and acceleration at t_n are known. Based on approximate solutions, the convergent solution of displacement, velocity, and acceleration at t_{n+1} are then derived by iterative calculation in Newton-Raphson method, which is employed for the solution for nonlinear simultaneous equations.

In the first step of iterative computation, approximate solution at t_{n+1} is computed through time integration method based on displacement, velocity and acceleration at t_n. Hence Eq. (4.1) can be rewritten as:

$$\mathbf{M}^{(0)}\ddot{\mathbf{q}}_{\mathbf{n+1}}^{(1)} + \mathbf{C}^{(0)}\dot{\mathbf{q}}_{\mathbf{n+1}}^{(1)} + \mathbf{K}^{(0)}\mathbf{q}_{\mathbf{n+1}}^{(1)} = \mathbf{F}_{\mathbf{ext,n+1}} - \bar{\mathbf{F}}_{\mathbf{n}}^{(0)} \tag{4.15}$$

where $\mathbf{M}^{(0)}$, $\mathbf{C}^{(0)}$ and $\mathbf{K}^{(0)}$ are mass, damping and stiffness matrices at t_n, respectively; $\bar{\mathbf{F}}_{\mathbf{n}}^{(0)}$ is nonlinear correction force, such as:

$$\bar{\mathbf{F}}_{\mathbf{n}}^{(0)} = \mathbf{F}_{\mathbf{cint,n}} + \mathbf{F}_{\mathbf{kint,n}} - \mathbf{C}^{(0)}\dot{\mathbf{q}}_{\mathbf{n}} - \mathbf{K}^{(0)}\mathbf{q}_{\mathbf{n}} \tag{4.16}$$

Note that at the first step of iterative computation, each matrix and nonlinear correction force are computed with $\ddot{\mathbf{q}}_{\mathbf{n}}$, $\dot{\mathbf{q}}_{\mathbf{n}}$ and $\mathbf{q}_{\mathbf{n}}$ at t_n. In Newmark-β method, displacement and velocity are given by:

$$\begin{aligned}
\dot{\mathbf{q}}_{\mathbf{n+1}} &= \dot{\mathbf{q}}_{\mathbf{n}} + h\{\gamma\ddot{\mathbf{q}}_{\mathbf{n+1}} + (1-\gamma)\ddot{\mathbf{q}}_{\mathbf{n}}\} \\
\mathbf{q}_{\mathbf{n+1}} &= \mathbf{q}_{\mathbf{n}} + h\dot{\mathbf{q}}_{\mathbf{n}} + h^2\left\{\left(\frac{1}{2}-\beta\right)\ddot{\mathbf{q}}_{\mathbf{n}} + \beta\ddot{\mathbf{q}}_{\mathbf{n+1}}\right\}
\end{aligned} \tag{4.17}$$

where h is the time step; β and γ are parameters. By substituting Eqs. (4.16) and (4.17) for Eq. (4.15), simultaneous equations to take acceleration $\ddot{\mathbf{q}}_{n+1}^{(1)}$ as an unknown are gained as:

$$\left[\mathbf{M}^{(0)} + h\gamma\mathbf{C}^{(0)} + h^2\beta\mathbf{K}^{(0)}\right]\ddot{\mathbf{q}}_{\mathbf{n+1}}^{(1)} = \mathbf{F}_{\mathbf{ext,n+1}} - \mathbf{F}_{\mathbf{cint,n}} - \mathbf{F}_{\mathbf{kint,n}} - h(1-\gamma)\mathbf{C}^{(0)}\ddot{\mathbf{q}}_{\mathbf{n}} - \mathbf{K}^{(0)}\left\{h\dot{\mathbf{q}}_{\mathbf{n}} + h^2\left(\frac{1}{2}-\beta\right)\ddot{\mathbf{q}}_{\mathbf{n}}\right\} \tag{4.18}$$

$\ddot{\mathbf{q}}_{n+1}^{(1)}$ can be derived from Eq. (4.18) and $\dot{\mathbf{q}}_{n+1}^{(1)}$, $\mathbf{q}_{n+1}^{(1)}$ from Eq. (4.17). In case displacement $\mathbf{q}_{n+1}^{(1)}$ is unknown, the same process is available by determining simultaneous equations to take $\mathbf{q}_{n+1}^{(1)}$ as unknown instead of Eq. (4.18). Since Eq. (4.1) is derived through linear approximation between t_n and t_{n+1}, $\ddot{\mathbf{q}}_{n+1}^{(1)}$, $\dot{\mathbf{q}}_{n+1}^{(1)}$ and $\mathbf{q}_{n+1}^{(1)}$ do not rigorously satisfy the equations of motion at t_{n+1}. Therefore, after the second step of iteration (l=2, 3,..) the approximate solution is corrected by

$$\begin{aligned}\mathbf{q}_{n+1}^{(\mathbf{l})} &= \mathbf{q}_{n+1}^{(\mathbf{l}\text{-}\mathbf{1})} + \delta\mathbf{q}^{(\mathbf{l})} \\ \dot{\mathbf{q}}_{n+1}^{(\mathbf{l})} &= \dot{\mathbf{q}}_{n+1}^{(\mathbf{l}\text{-}\mathbf{1})} + \delta\dot{\mathbf{q}}^{(\mathbf{l})} \\ \ddot{\mathbf{q}}_{n+1}^{(\mathbf{l})} &= \ddot{\mathbf{q}}_{n+1}^{(\mathbf{l}\text{-}\mathbf{1})} + \delta\ddot{\mathbf{q}}^{(\mathbf{l})}\end{aligned} \tag{4.19}$$

An equation of equilibrium at t_{n+1} is expressed as:

$$\mathbf{F}_{\mathbf{iner,n+1}} + \mathbf{F}_{\mathbf{cint,n+1}} + \mathbf{F}_{\mathbf{kint,n+1}} = \mathbf{F}_{\mathbf{ext,n+1}} \tag{4.20}$$

By substituting Eq. (4.18) for Eq. (4.20), performing Taylor expansion around the quantities at the l-1 step of iteration $\ddot{\mathbf{q}}_{n+1}^{(\mathbf{l}\text{-}\mathbf{1})}$, $\dot{\mathbf{q}}_{n+1}^{(\mathbf{l}\text{-}\mathbf{1})}$ and $\mathbf{q}_{n+1}^{(\mathbf{l}\text{-}\mathbf{1})}$, and taking first-order term of Taylor expansion, following equation is derived:

$$\mathbf{M}^{(\mathbf{l}\text{-}\mathbf{1})}\delta\ddot{\mathbf{q}}^{(\mathbf{l})} + \mathbf{C}^{(\mathbf{l}\text{-}\mathbf{1})}\delta\dot{\mathbf{q}}^{(\mathbf{l})} + \mathbf{K}^{(\mathbf{l}\text{-}\mathbf{1})}\delta\mathbf{q}^{(\mathbf{l})} = \mathbf{F}_{\mathbf{ext,n+1}} - \mathbf{F}_{\mathbf{iner,n+1}}^{(\mathbf{l}\text{-}\mathbf{1})} - \mathbf{F}_{\mathbf{cint,n+1}}^{(\mathbf{l}\text{-}\mathbf{1})} - \mathbf{F}_{\mathbf{kint,n+1}}^{(\mathbf{l}\text{-}\mathbf{1})} \tag{4.21}$$

where $\mathbf{M}^{(\mathbf{l}\text{-}\mathbf{1})}$, $\mathbf{C}^{(\mathbf{l}\text{-}\mathbf{1})}$, $\mathbf{K}^{(\mathbf{l}\text{-}\mathbf{1})}$, $\mathbf{F}_{\mathbf{iner,n+1}}^{(\mathbf{l}\text{-}\mathbf{1})}$, $\mathbf{F}_{\mathbf{cint,n+1}}^{(\mathbf{l}\text{-}\mathbf{1})}$ and $\mathbf{F}_{\mathbf{kint,n+1}}^{(\mathbf{l}\text{-}\mathbf{1})}$ are determined based on the quantities at the l-1 step of iteration $\ddot{\mathbf{q}}_{n+1}^{(\mathbf{l}\text{-}\mathbf{1})}$, $\dot{\mathbf{q}}_{n+1}^{(\mathbf{l}\text{-}\mathbf{1})}$ and $\mathbf{q}_{n+1}^{(\mathbf{l}\text{-}\mathbf{1})}$. From Eqs. (4.17) and (4.18), I derive

$$\begin{aligned}\delta\ddot{\mathbf{q}}^{(\mathbf{l})} &= h\gamma\delta\ddot{\mathbf{q}}^{(\mathbf{l})} \\ \delta\mathbf{q}^{(\mathbf{l})} &= h^2\beta\delta\ddot{\mathbf{q}}^{(\mathbf{l})}\end{aligned} \tag{4.22}$$

By substituting Eq. (4.22) for Eq. (4.21), simultaneous equations about $\delta\ddot{\mathbf{q}}^{(\mathbf{l})}$ is gained as:

$$\left[\mathbf{M}^{(\mathbf{l}\text{-}\mathbf{1})} + h\gamma\mathbf{C}^{(\mathbf{l}\text{-}\mathbf{1})} + h^2\beta\mathbf{K}^{(\mathbf{l}\text{-}\mathbf{1})}\right]\delta\ddot{\mathbf{q}}^{(\mathbf{l})} = \mathbf{F}_{\mathbf{ext,n+1}} - \mathbf{F}_{\mathbf{iner,n+1}}^{(\mathbf{l}\text{-}\mathbf{1})} - \mathbf{F}_{\mathbf{cint,n+1}}^{(\mathbf{l}\text{-}\mathbf{1})} - \mathbf{F}_{\mathbf{kint,n+1}}^{(\mathbf{l}\text{-}\mathbf{1})} \tag{4.23}$$

Eq. (4.23) is solved to determine $\delta\ddot{\mathbf{q}}^{(\mathbf{l})}$ and Eq. (4.22) to determine $\delta\dot{\mathbf{q}}^{(\mathbf{l})}$ and $\delta\mathbf{q}^{(\mathbf{l})}$. $\ddot{\mathbf{q}}_{n+1}^{(\mathbf{l}\text{-}\mathbf{1})}$, $\dot{\mathbf{q}}_{n+1}^{(\mathbf{l}\text{-}\mathbf{1})}$ and $\mathbf{q}_{n+1}^{(\mathbf{l}\text{-}\mathbf{1})}$ are then determined with Eq. (4.18). Iterative computation at each time step is conducted until the residual of force at each node is within the range of certain tolerance.

Using these formularization and time integration techniques, a three-dimensional flexible beam model was applied to a flexible body dynamics (FBD) solver which can analyze of the six-degrees of freedom (6DoF) flight and passive body flexions of a flying hawkmoth. The flexible beam model is located on the central axis of the body grid and the wing-base of the right and left wing grids as depicted in Fig. 4.5A. Note that the beam elements located on the central axis was divided into three part of the head, the thorax and the abdomen and the mass of each part was determined based on the measurement of the hawkmoth *Manduca sexta*, by Hedrick and Daniel (2006) as shown in Table 1. In addition, note that the aerodynamic forces on the wings act to the two wing base nodes. The governing equation is formulated on the basis of update reference frame method, which is included in the finite element method. In this method, the nonlinear restoring force and stiffness matrix are calculated on a basis of small deformation theories. The governing equation of the FBD solver is expressed as

$$\boldsymbol{M\ddot{q} + C\dot{q} + K_L q + f_{int}(q) - f_{ext} = 0} \tag{4.24}$$

where $\boldsymbol{M}$ expresses the lumped mass matrix, $\boldsymbol{C}$ the damping matrix, $\boldsymbol{K_L}$ the linear stiffness matrix, $\boldsymbol{f_{int}}$ the nonlinear restoring force, $\boldsymbol{f_{ext}}$ the external force, and $\boldsymbol{q}$ the positions and orientations in the global frame. Note that in the present study, each element changes the position not only by the deformation but also by the whole-body motion. Thus the restoring force is expressed as a nonlinear function of the displacement. For the integration, Newmark-β for nonlinear problems was used. The tangent stiffness matrix $\boldsymbol{K_N}$ for the time integration is expressed as the partial derivative of $\boldsymbol{f_{int}}$ as

$$\boldsymbol{K_N = \partial f_{int} / \partial q} \tag{4.25}$$

The $\boldsymbol{K_N}$ can be divided into two parts as

$$\boldsymbol{K_N = K_G + K_O} \tag{4.26}$$

where $\boldsymbol{K_G}$ is the geometric stiffness matrix and $\boldsymbol{K_O}$ is the elastic deformation matrix.

The CFD solver and the FBD solver need to exchange information to achieve the coupled computation. I used the following manner for this coupling process (Piperno and Farhat, 2001), as shown in Fig. 4.6. (1) Predict the displacement of each node of the structural model at time t_{n+1}, using the information (displacement, velocity and acceleration) at time t_n; (2) Update the position of the fluid grid based on the increments of each node; (3) Transfer fluid force to the structure; and (4) advance the time in the FBD solver.

Note that the computational fluid dynamics solver used in this study is the same that of section 2.2.3, however the background grid is changed for translation of the wing and body grids. In this study, a Cartesian grid is adopted as the background and the global grid as shown in Fig. 4.7A. More detail about the CFD solver, including the techniques about the multi-blocked and overset-grid system can be found in Liu (2009) and Maeda and Liu (2013).

4.2.3 Active and passive body models

Firstly, in order to see the effect of the active body flexion on flight dynamics, I constructed body models with a static flexion based on the measurement of the active body flexion under the visual stimuli by Dyhr, et al. (2013). Figure 4.8A-C show the three body models that have a straight body, a convex body and a concave body, respectively. Note that the abdominal angle of the convex and concave body models is adjusted to be approximately 15° and -15°. Moreover, the differences of the moment of inertia in the pitch direction due the change of these abdominal angles are less than 0.5 percent of the value of that of the straight body model. The center of mass (CoM) position in each body model is also shown in Fig. 4.8D. Note that the CoM position was calculated based on the masses and positions of all the nodes in global coordinate system such as:

$$x_G = \frac{\sum_{i=1}^{n} m_i\, x_i}{\sum_{i=1}^{n} m_i}\,, y_G = \frac{\sum_{i=1}^{n} m_i\, y_i}{\sum_{i=1}^{n} m_i},\quad z_G = \frac{\sum_{i=1}^{n} m_i\, z_i}{\sum_{i=1}^{n} m_i} \tag{4.4}$$

where mi expresses the mass of each node and x_i, y_i, z_i the positions of each node in

the global coordinate system. Note that in this study, the number of all the nodes, including the wing base nodes is 43.

In this study, the active body flexion is assumed to be static. Accordingly, the flight dynamics with active body flexion is simulated under the high stiffness condition in which I can treat the body as a rigid body model without passive abdominal flexion. Such conditions are achieved by changing the Young's modulus of all elements to 1.0×10^5 MPa. Furthermore, with consideration of minimizing the influence of the wing kinematics on flight dynamics to accurately evaluate the active body flexion, I performed all the simulations after an appropriate tuning of the wing kinematics. More details are given in section 4.2.4.

Furthermore, I carried out an extended study on the effect of the dynamic-and passive-body flexion on flight dynamics by changing the Young's moduli at the three joint elements between thorax and abdomen of E_{j0} and E_{j1} with $E_{j1} = 2E_{j0}$ (Fig. 4.5B). Here E_{j0} are set to be 0.025, 0.030, 0.045 and 0.1 MPa, respectively. The Young's modulus $E_{j0} = 1.0\times10^5$ MPa was chosen for a rigid body model as used for the active body flexion and was distributed uniformly across each cross section.

4.2.4 Flight control system

For a pure evaluation of the effect of active body flexion, the wing kinematics was refined to realize that the cycle-averaged thoracic angle of the straight body model (Fig. 4.8A) is capable to maintain the initial thoracic angle $\theta_t = 40°$ during free-flight. This 'designable' wing kinematics was constructed *via* an *in-house* PD (Proportional-Derivative) flight control system, which was originally developed by Gao (2011). The configuration of the flight c 1 ontrol system is illustrated in Fig. 4.9. In this control system, errors between the sensed body attitude/position and the desired values that are set as the hovering conditions are fed back to the PD controller at the end of each wingbeat cycle. For the sensed data, I take the last-period-averaged values of the body position, the attitude, and the time derivative. The PD control algorithm is expressed as :

$$O_w = K_p e(t) + K_D \frac{d}{dt} e(t) \tag{4.5}$$

where O_w is the output values which are treated as the wing kinematic parameters; K_P is proportional gain; K_D is derivative gain; and $e(t)$ is the error between the current attitude/position and the desired value. The output obtained from the controller is a set of slightly modified wing kinematics for the next wingbeat cycle, which is forwarded to the CFD solver as the input. Then a fluid-structure interaction (FSI) problem based on the CFD and FBD coupling is solved with the refined kinematics parameters. Note that the parameters used for longitudinal control are positional angle, feathering angle, stroke plane angle and flapping frequency.

The body position and its attitude are fixed in the first wing beat as a tethered model but are released after then so as to perform the free-flight. Note that the refined wing kinematics and the transition from tethered flight to free-flight are adopted only to the active body flexion analysis.

4.3 Results and Discussion

4.3.1 Refined wing kinematics *via* flight control system

The refined wing kinematics are constructed using the averaged values during the period where can be treated as the hovering flight. Figure 4.10 shows the time course of the thoracic angle (Fig. 4.10A) and the trajectory of CoM in X-Z plane (Fig. 4.10B). It is seen that the stable state of the time course of thoracic angle after the 4th wingbeat cycle and the elliptical trajectory of the CoM during the period of t/T = 7 to 9. It is also seen that these condition are achieved in the different attitude and position from the initial attitude and position which are given to flight control system as the desired values. This is mainly due to the steady-state deviation and more accurate trimmed flight can be achieved with introducing PID control system. Moreover, it is seems that more exhaustive gain adjustment is required for more accurate trimmed flight because there are small oscillation of the cycle-averaged thoracic angle over the stable state. Although these results show room for improvement on the current control system, I adopted the averaged wing kinematics during the 8th and 9th wing beat cycle as the refined wing kinematics. The refined wing kinematics are illustrated in Fig. 4.11. Note that the refined stroke plane angle and frequency are 23.4° and 22.4 Hz, respectively.

4.3.2 Effect of active body flexion

Our computational results indicate that active body flexion in terms of variations in body posture can lead to pronounced changes in body attitude. Figure 4.12 shows the comparisons of the time courses of aerodynamic pitching torques acting on wings and body (Fig. 4.12A) and the time-averaged aerodynamic torques (Fig. 4.12B) among three models with different CoMs. It is seen that the positive and negative aerodynamic torques apparently correspond with the pitch-up and pitch-down of the body. The influence of these aerodynamic torques on the body attitude is further illustrated in Figure 4.13A and B in terms of the time courses of thoracic angles and the time-averaged thoracic angles over the 3rd wingbeat cycle. As shown in Fig. 4.12A,

there are peaks observed in the time courses of aerodynamic torques before and after the stroke reversal. It is seen that, even though the flapping wings generate the majority of the total aerodynamic torque, the body flexion also has an effect on the total aerodynamic torque as can be seen in the time-averaged values (Fig. 4.12B) because the shifts of the CoM position (Fig. 4.8D) leads to a change in the length of moment arm to each flapping wing. Note that the rate of the aerodynamic torque generated by the each body is less than 1 percent of the total aerodynamic torque in all three cases. It is also seen that there is the considerable difference of the time-averaged value of the aerodynamic torque from zero value in the straight body model (Fig. 4.12B), this may be due to the disappearance of the damping effect on the interaction between the moving body and flapping wings in tethered flight.

Moreover, it is seen that the concave body leads to reducing the aerodynamic torques compared to the straight body model at supination while keeping the aerodynamic torque unchanged at pronation. Interestingly, while the straight body model generates a slight time-averaged pitch-up torque under tethered condition, the concave body model generates a 60 percent larger time-averaged torque, resulting in a significant pitch-up within a few wingbeat cycles of free-flight (Fig. 4.13A-B). On the other hand, the convex body can generate a pitch-down torque in a manner of time-averaged because the aerodynamic torque is reduced at pronation, which results in a rapid pitch-down in free-flight.

4.3.3 Effect of passive body flexion

Furthermore, our computational results of passive body flexion show that the body flexibility can affect the body attitude. Figure 4.13A and B show the time courses of the thoracic and abdominal angles with flexible bodies. The time-averaged thoracic angle and the amplitude of the oscillation of abdominal angle over the 5th cycle are also shown in Fig. 4.15A and B. It is seen that the thoracic angle is increased with decreasing stiffness from 0.1 MPa, and, interestingly, is decreased again when the body is more flexible than 0.03MPa. This nonlinearity is thought to be due to the non-linear

resonance which is demonstrated by the previous studies with flexible wings (Eldredge, et al., 2010, Mountcastle and Daniel, 2010). I am not going to discuss the detail of such phenomenon because of the complexity of the current model that simulates the interactions between aerodynamics, structural dynamics and flight dynamics. It is also seen that while the thoracic angle of the rigid abdomen is slightly increased with time and reaches 50 degree after 4 wingbeat cycles, the body with less flexible joint (E_{j0} = 0.1 MPa) is mostly stable, maintaining its initial thoracic angle throughout the free-flight simulation (Fig. 4.14A, Fig. 4.15A).

With respect to the abdominal angle, I see a feature of scattering oscillation with high-frequency components in each flexible body model, which is likely a result of resonance. However, it is also observed that the oscillating amplitude seems to be increased with decreasing stiffness within the range defined here (Fig. 4.15B). Note that the abdominal angles of all flexible bodies are calculated to be less than 7 degree at highest, which are much smaller than those of the active body flexion case. Such deformations (Fig. 4.14B), however, can significantly affect the flight dynamics of hawkmoth hovering. It is still unclear yet whether such body flexibility plays a positive role in stabilizing the body dynamics, or merely result in some pitch-up or pitch-down of the body. In either case, it is of highly non-linear behaviors that are very likely associated with the interactions of aerodynamics and the flight dynamics of the flyer.

4.4 Summary

Flapping-wing flyers are subject to the inherent instabilities in their flight dynamics (Sun, et al., 2007). In this study, I have studied the effects of active and passive body flexion on flight dynamics by using *in-house* CFD and FBD solvers. Our computational results with active body flexion indicate that the body flexion has a significant impact on the flight dynamics: while the convex or concave body flexion lead to a slight change of CoM less than 2 percent of the body length, such a change obviously results in a pronounced variation in body attitude within a few wing beat cycles. This points out that the CoM position can be a sensitive parameter in the analysis of flight dynamics

and control of a flapping-wing flight, which may in case dominate the nature of maneuverability and flight stability. Furthermore, the free-flight simulations with flexible body models reveal that the body flexibility of a flapping-wing flyer can generate some pitch-up and pitch-down in a more complicated way than the steady body flexion, and, in particular, the abdominal oscillation very likely play a role in enhancing the flight stability.

Furthermore, our results point to the potential and usefulness of the body flexion in designing a bio-inspired flapping-wing MAV. Taking into account the mechanisms of active / passive body flexion may be able to let us simplify the control system in flapping-wing flights, which can be achieved by adjusting high-speed flapping-wing motions.

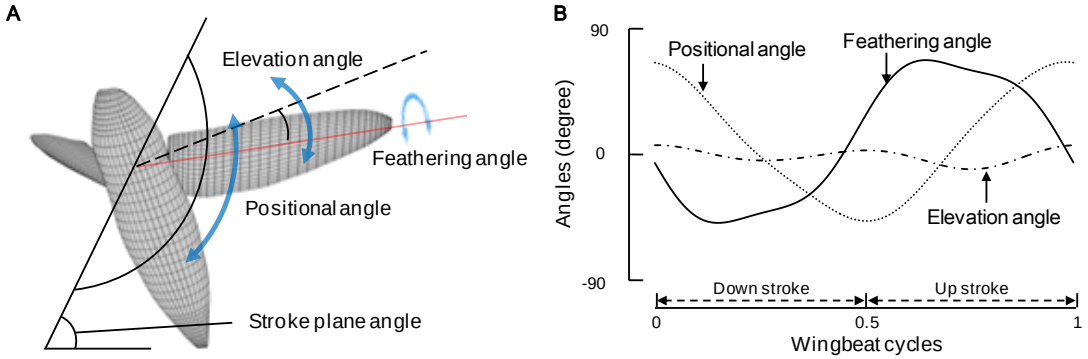

Fig. 4.1 (A) Definition of three-dimensional movement of a flapping wing. (B) Wing kinematics of a hovering hawkmoth.

Table 4.1 Parameters used for computational analysis

Total mass, m (mg)	1591	
Head, m_h (mg)	107	
Thorax, m_t (mg)	596	
Abdomen, m_a (mg)	818	
Single wing mass, m_w (mg)	35	
Mean chord length, c_m (mm)	18.6	
Wing length, R (mm)	48.8	
Wingbeat frequency, f (Hz)	26.0	
Wingbeat amplitude, Φ (rad)	1.71	
Initial stroke plane angle χ (deg)	24.0	
Density of air, ρ (Kg/m^3)	1.225	
Kinematic viscosity of air, ν (m^2/s)	1.5×10^{-5}	
Reference velocity, U_{ref} (m/s)	4.34	($U_{ref} = 2\Phi Rf$)
Reduced frequency, k (-)	0.35	($k = 2\pi f c_m/U_{ref}$)
Reynolds number, Re (-)	5382	($Re = U_{ref}\, c_m/\nu$)

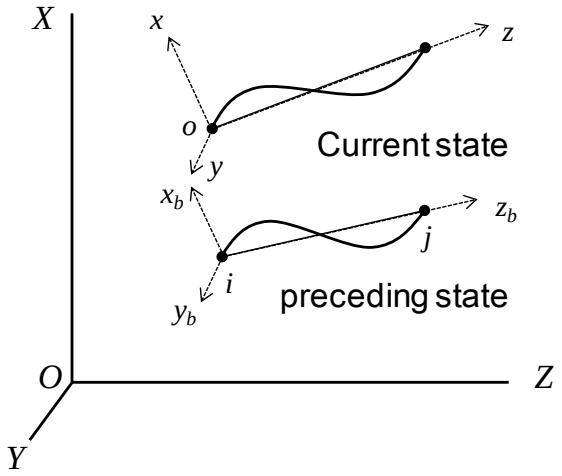

Fig. 4.2 The orthogonal reference frame and the element reference frame.

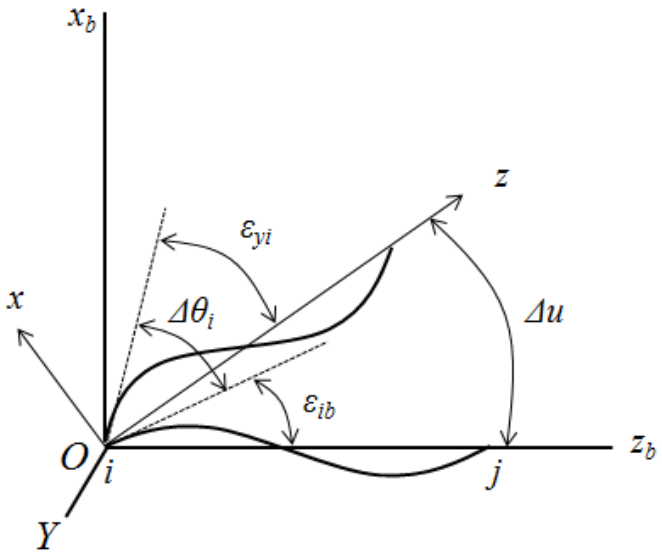

Fig. 4.3 Angles between current state and preceding state around y-axis.

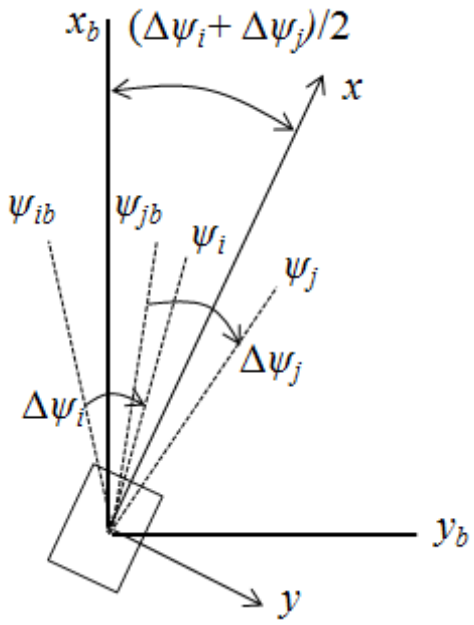

Fig. 4.4 Angular displacement around z_b-axis.

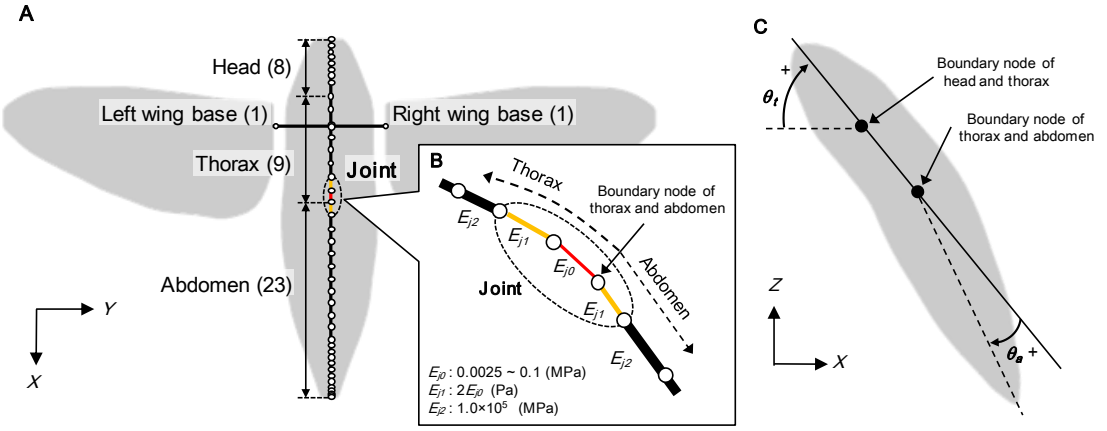

Fig. 4.5 (A) Schematic of the nodes and the beam elements. Note that the element number of each part is also displayed in parentheses. (B) Schematic of the beam elements around the joint between the thorax and abdomen. Young's modulus of the middle joint element (red) is termed E_{j0} and each side joint elements (orange) are termed E_{j1}. All the other elements are termed E_{j2} and given the same Young's modulus. (C) Definition of thoracic angle θ_t and abdominal angle θ_a. Note that thoracic angle θ_t is measured from the horizon.

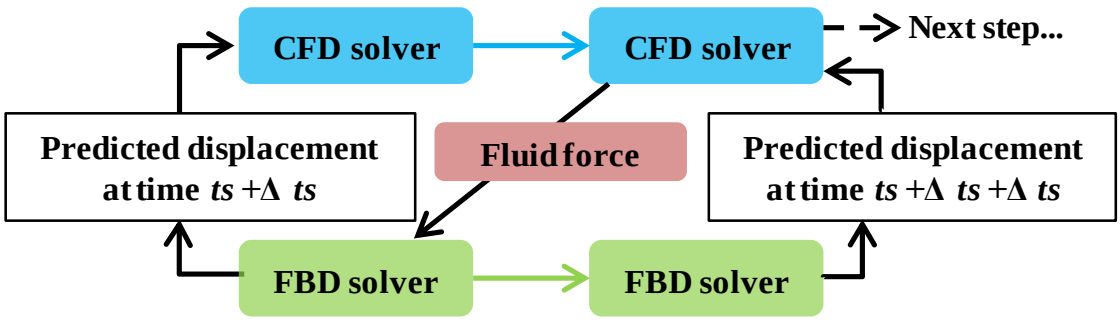

Fig. 4.6. Configuration of coupling method using predicted value.

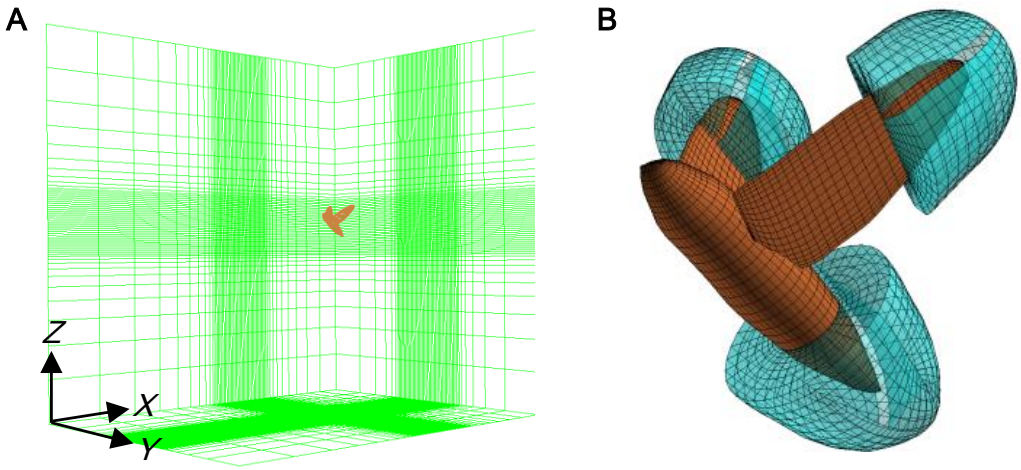

Fig. 4.7 Grid system. (A) Global grid blocks for fluid dynamics simulation with global coordinate system (X, Y, Z). (B) Grids of a hawkmoth model.

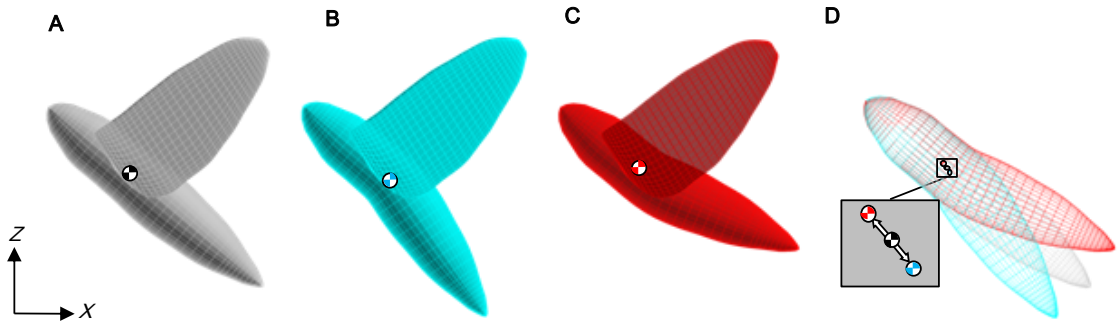

Fig. 4.8 Active body models with static flexions. The body models are defined as: (A) The straight body model (Gray); (B) The convex body model (blue); and (C) The concave body model (red). (D) Modified center of mass in each body model due to the change of abdominal angle.

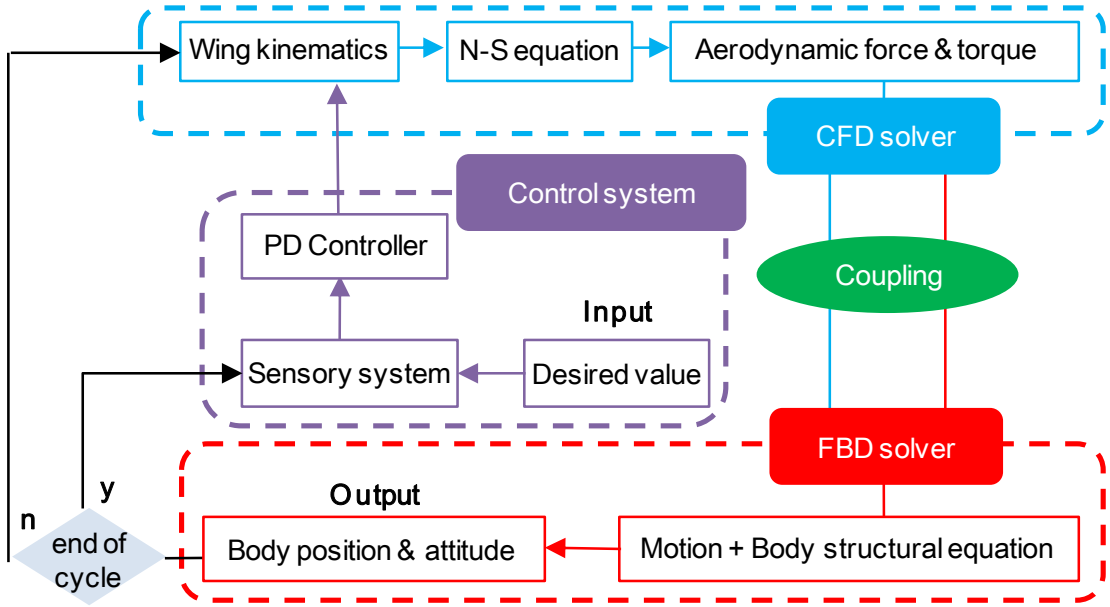

Fig. 4.9 Configuration of PD (Proportional- Derivative) control system.

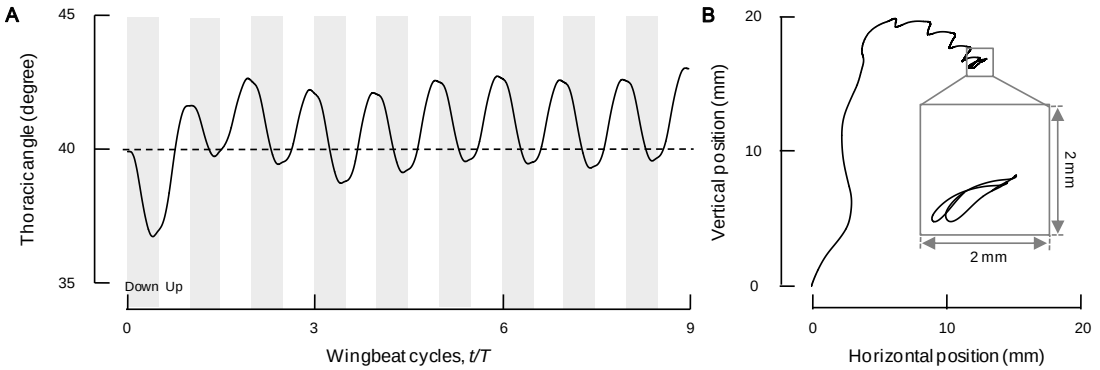

Fig. 4.10 Computational results of free flight with straight body model *via* flight control system. (A) Time course of thoracic angle. (B) Trajectory of CoM in the X-Z plane, starting from origin at t/T = 0. Magnified region indicate the period during t/T = 7 to 9.

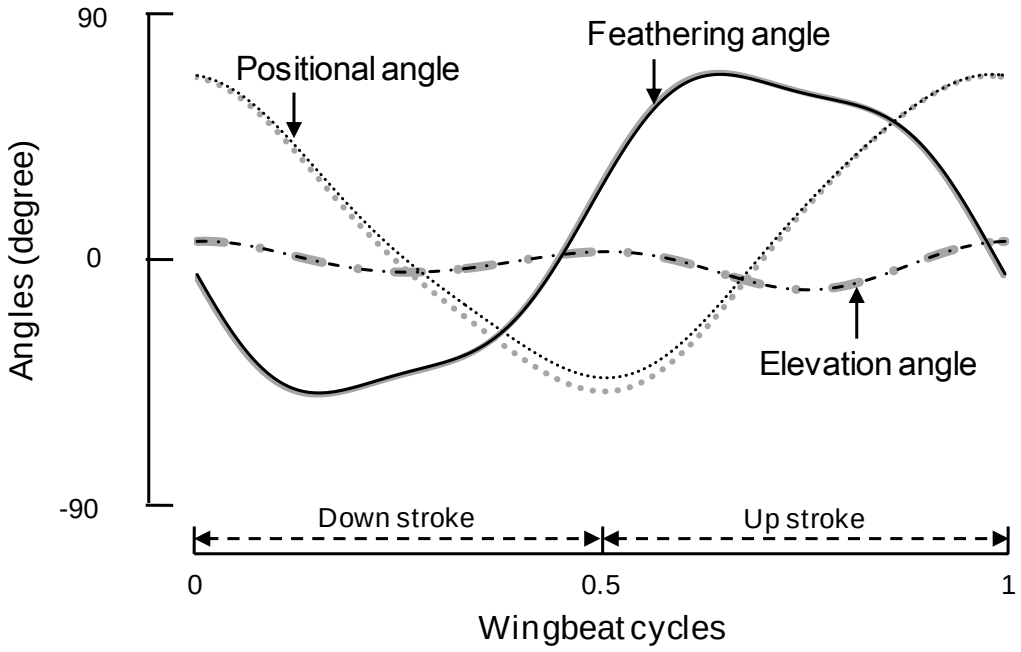

Fig. 4.11 Refined wing kinematics (black) *via* flight control system. The initial wing kinematics (gray) is also plotted for comparison.

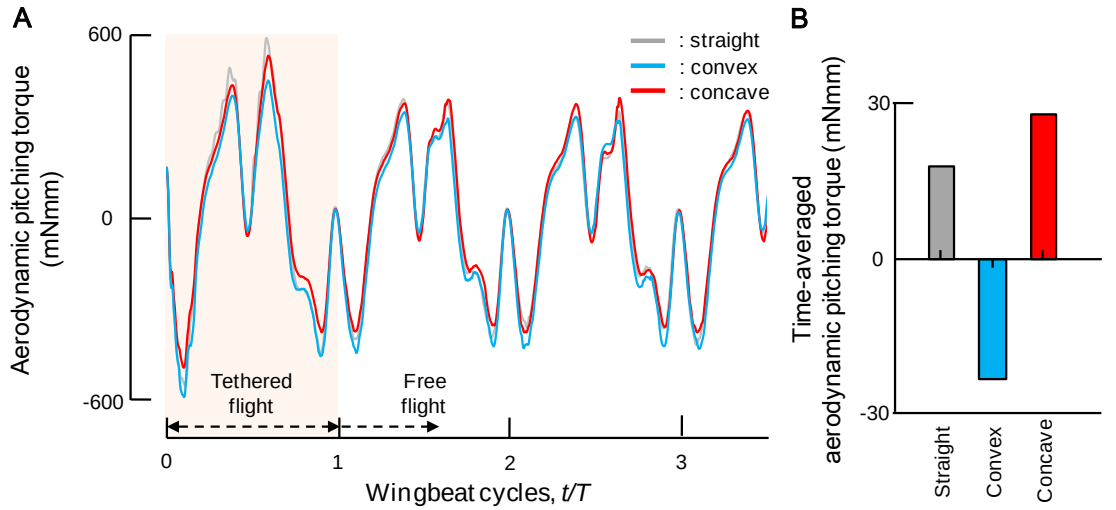

Fig. 4.12 Computational results of active body models. (A) Time courses of the CoM-based aerodynamic pitching torques. (B) Time-averaged aerodynamic pitching torques over the 1st (tethered) wing beat cycle.

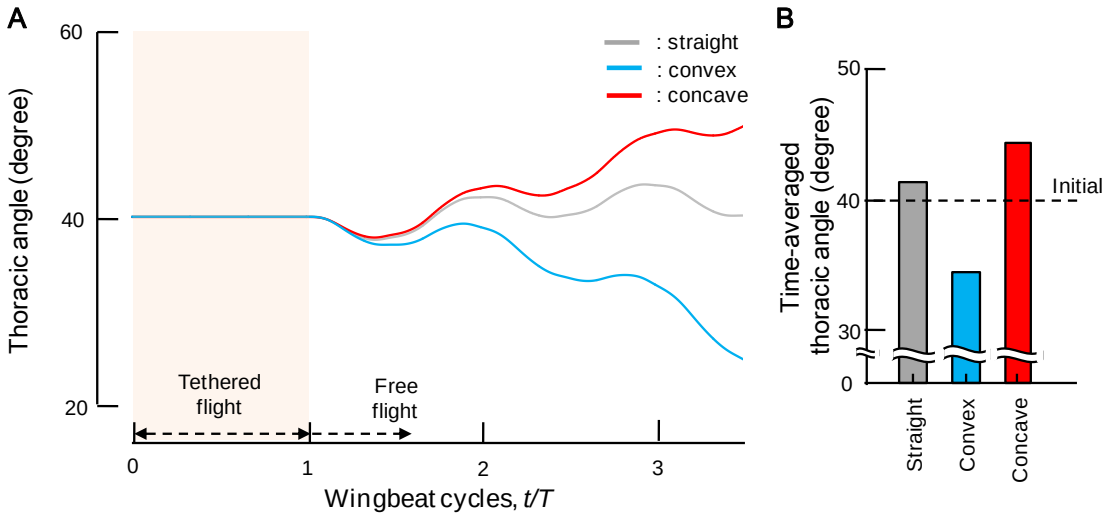

Fig. 4.13 Computational results of active body models. (A) Time courses of thoracic angles. (B) Time-averaged thoracic angles over the 3rd wingbeat cycle.

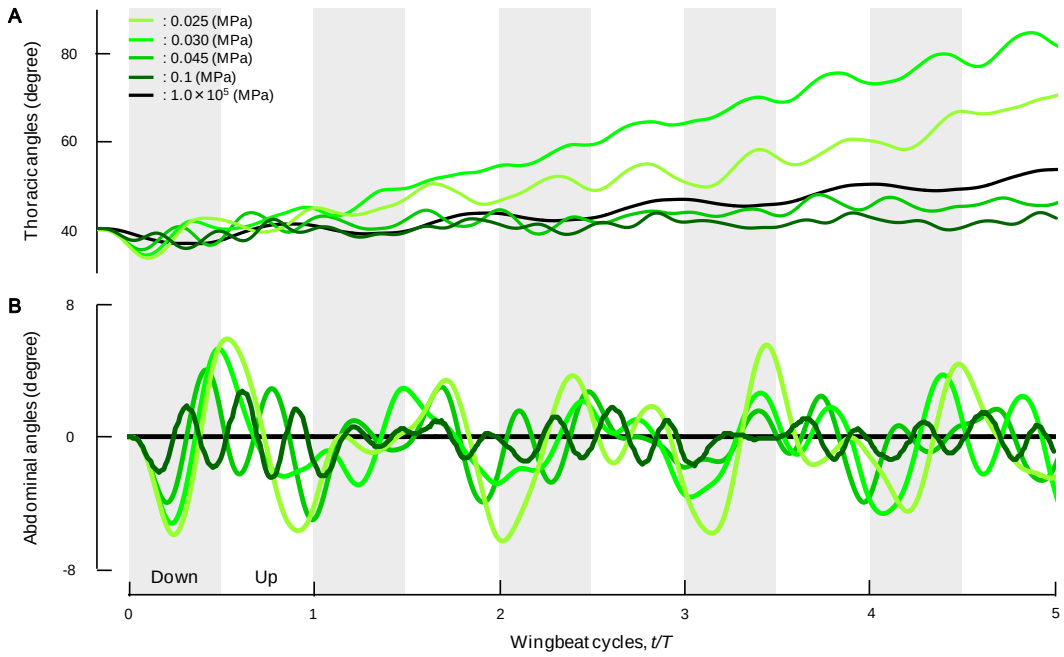

Fig. 4.14 Computational results of passive body models. Time courses of (A) thoracic angles and (B) abdominal angles. Shaded area corresponds to downstroke of each wingbeat cycle.

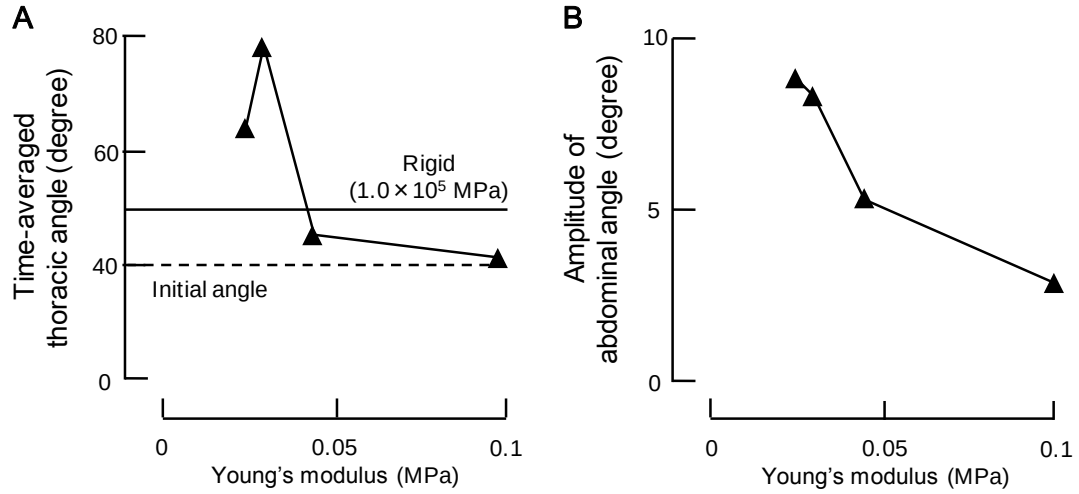

Fig. 4.15 Computational results of passive body models. (A) Time-averaged thoracic angle over the 5th wingbeat cycle. Note that the value of that of rigid body model is also shown. (B) Amplitude of the oscillation of abdominal angle over the 5th wingbeat cycle.

Reference

Aono, H. and Liu, H., Vortical structure and aerodynamics of hawkmoth hovering, Journal of Biomechanical Science and Engineering, Vol. 1, pp. 234–245 (2006)

Baader, A., The posture of the abdomen during locust flight: regulation by steering and ventilatory interneurones, The Journal of Experimental Biology, Vol. 151, pp. 109-131 (1990)

Camhi, J. M., Sensory control of abdominal posture in flying locusts, The Journal of Experimental Biology, Vol. 52, pp. 533–537 (1970)

Dyhr, J. P., Morgansen, K. A., Daniel, T. L. and Cowan, N. J., Flexible strategies for flight control: an active role for the abdomen, The Journal of Experimental Biology, Vol. 216, pp. 1523–1536 (2013)

Eldredge, J. D., Toomey, J. and Medina, A., On the roles of chord-wise flexibility in a flapping wing with hovering kinematics, Journal of Fluid Mechanics, Vol. 659, pp. 94-115 (2010)

Fry, S. N., Sayaman, R. and Dickinson, M. H., The aerodynamics of free-flight maneuvers in Drosophila, Science, Vol. 300, pp. 495-498 (2003)

Frye, M. A., Effect of stretch receptor ablation on the optomotor control of lift in the hawkmoth Manduca sexta, The Journal of Experimental Biology, Vol. 204, pp. 3683-3691 (2001)

Gao, N., A numerical study of passive and active control in insect hovering, Chiba University PhD thesis (2011).

Götz, K. G., Hengstenberg, B. and Biesinger, R., Optomotor control of wing beat and body posture in Drosophila, Biological Cybernetics, Vol. 35, pp. 101–112 (1979)

Hedrick, T. L. and Daniel, T. L., Flight control in the hawkmoth Manduca sexta: the inverse problem of hovering, The Journal of Experimental Biology, Vol. 209, pp. 3110–3114 (2006)

Hinterwirth, A. J. and Daniel, T. L., Antennae in the hawkmoth Manduca sexta (Lepidoptera, Sphingidae) mediate abdominal flexion in response to mechanical stimuli, Journal of Comparative Physiology A, Vol. 196, pp. 947–956 (2010)

Kammer, A. E., The motor output during turning flight in a hawkmoth, Maduca sexta, Journal of Insect Physiology, Vol. 17, pp 1073-1086 (1971)

Kim, J.K. and Han, J. H., A multibody approach for 6-DOF flight dynamics and stability analysis of the hawkmoth Manduca sexta, Bioinspiration & Biomimetics, Vol.9, 016011 (2014)

Liu, H., Integrated modeling of insect flight: from morphology, kinematics to aerodynamics, Journal of Computational Physics, Vol. 228, pp. 439–459 (2009)

Liu, H., Ellington, C. P., Kawachi, K., Van den Berg, C. and Willmott, A.P., A computational fluid dynamic study of hawkmoth hovering, The Journal of Experimental Biology, Vol. 201, pp. 461–477 (1998a)

Liu, H. and Kawachi, K., A numerical study of insect flight, Journal of Computational Physics, Vol. 146, pp. 124–156 (1998b)

Luu, T., Cheung, A., Ball, D. and Srinivasan, M. V., Honeybee flight: a novel 'streamlining' response, The Journal of Experimental Biology, Vol. 214, 2215-2225 (2011)

Maeda, M. and Liu, H., Ground effect in fruit fly hovering: a three-dimensional computational study, Journal of Biomechanical Science and Engineering, Vol. 8, pp. 344–355 (2013)

Mountcastle, A. M. and Daniel, T. L., Vortexlet models of flapping flexible wings show tuning for force production and control, Bioinspiration & Biomimetics, Vol. 5, 045005 (2010)

Piperno, S. and Farhat, C., Partitioned procedures for the transient solution of coupled aeroelastic problems‐part ii : energy transfer analysis and three-dimensional applications, Comput. Methods Appl. Mech. Eng., vol. 190, pp 3147-3170 (2001)

Sun, M., Wang, J. and Xiong, Y., Dynamic flight stability of hovering insects, Acta Mechanica Sinica, Vol. 23, pp. 231-246 (2007)

Taylor, G. K., Mechanics and aerodynamics of insect flight control, Biological Reviews, Vol. 76, pp. 449-471 (2001)

Willmott, A. P. and Ellington, C. P., The mechanism of flight in the hawkmoth Manduca sexta. I. kinematics of hovering and forward flight, The Journal of Experimental Biology, Vol. 200, pp. 2705–2722 (1997)

Wu, J. H., Zhang, Y. L. and Sun, M., Hovering of model insects: simulation by coupling equations of motion with Navier-Stokes equations, The Journal of Experimental Biology, Vol. 212, pp. 3313-3329 (2009)

Yokoyama, N., Senda, K., Iima, M. and Hirai, N., Aerodynamic forces and vortical structures in flapping butterfly's forward flight, Physics of Fluids, Vol. 25, 021902 (2013)

Zhanker, J. M., How does lateral abdomen deflection contribute to flight control of Drosophila melanogaster, Journal of Comparative Physiology A, Vol. 162, pp. 581–588 (1988)

Japan Society of Mechanical Engineers, Multibody dynamics (1) -Fundamental Theory-, pp. 232-234, Corona publishing (2006)

Japan Society of Mechanical Engineers, Multibody dynamics (1) -numerical analysis and its application-, pp. 108-165, Corona publishing (2007)

Chapter 5
Conclusions and future tasks

5.1 Concluding remarks

In the present paper, the flexibility of the wing and body of insects are focused and these effect on the aerodynamic performance and flight dynamics were studied with a bio-inspired numerical flight simulator. Moreover, the experimental study about filming of a hovering hawkmoth, *Agrius convolvuli* with the wing deformation and body flexion was conducted with high-speed video cameras.

Firstly, as a simplified model for flapping wings, the revolving wing model was constructed and studied numerically for elucidating the novel mechanisms associated with flexible flapping wings in Chapter 2.

Secondly, measuring and modeling wing deformation of a hovering hawkmoth, *Agrius convolvuli* were conducted with high-speed video cameras for reconstructing the dynamically morphing wing model with sufficient precision in Chapter 3.

Finally, a flexible body dynamics solver was developed and coupled with an *in-house* computational fluid dynamics solver. Using this integrated simulator, the effect of flexibility of the body during flapping flight was studied in Chapter 4.

It was revealed that the flexibility of insect's wing and body work effectively on the aerodynamics, flight efficiency, flight dynamics and flight stability in a separate way. Moreover, these results point to the potential and usefulness of the wing and body flexibility in designing a bio-inspired flapping-wing MAVs.

5.2 Future tasks

In the study of the insect's flight dynamics and flight stability with a computational approach, because of the complexity of nonlinear interaction between aerodynamics and structural dynamics, the wing and body models are treated as a rigid models in most cases. In this paper, the effect of the flexibility of the wing and body are evaluated separately in terms of the aerodynamic performances of the flexible wing and the flight stability of the flexible body.

Firstly, to aim at reproducing the realistic insect free flight with flexible wing and body in the computational analysis, the computational fluid dynamics solver for the wing and body aerodynamics, the computational structural dynamics solver for the wing and the flexible body dynamics solver will be coupled with manner of loose and the development of the newly bio-inspired simulator will be conducted.

Secondly, using this simulator, the nonlinear flight stability with the flexible wing and body will be performed for revealing the effect of the flexibility on the flight stability. There are some reports that insects have inherent instability in pitch direction and they require the active neural feedback for stabilization in a computational analysis of the rigid models. However, there is a possibility that the inherent stability of insects enhance their flight stability and analysis of these effects with a computational approach will make it clear quantitatively.

Finally, these results will apply to the designing of a flapping-winged MAVs and the development of the newly MAVs which have high stability to a gust of wind and high maneuverability will be conducted.